Science of Remote Sensing 7 (2023) 100074

Contents lists available at ScienceDirect

Science of Remote Sensing

journal homepage: www.sciencedirect.com/journal/science-of-remote-sensing

Improved terrain estimation from spaceborne lidar in tropical peatlands using spatial filtering

Alexander R. Cobb [a,*], René Dommain [b,c], Rahayu S. Sukri [d], Faizah Metali [e], Bodo Bookhagen [f], Charles F. Harvey [a,g], Hao Tang [h]

[a] Center for Environmental Sensing and Modeling, Singapore-MIT Alliance for Research and Technology, 138602, Singapore
[b] Asian School of the Environment, Nanyang Technological University, 639798, Singapore
[c] Human Origins Program, National Museum of Natural History, Smithsonian Institution, Washington, DC, 20013, USA
[d] Institute for Biodiversity and Environmental Research, Universiti Brunei Darussalam, Bandar Seri Begawan, BE1410, Brunei Darussalam
[e] Environmental and Life Sciences Programme, Universiti Brunei Darussalam, Bandar Seri Begawan, BE1410, Brunei Darussalam
[f] Institute of Geosciences, University of Potsdam, 14476, Potsdam, Germany
[g] Department of Civil and Environmental Engineering, Massachusetts Institute of Technology, Cambridge, MA, 02139, USA
[h] Department of Geography, National University of Singapore, 117570, Singapore

ARTICLE INFO

Keywords:
Tropical peatlands
Spaceborne laser altimetry
Ground point classification
Aerial laser scanning
ATLAS
GEDI
Spatial filter

ABSTRACT

Tropical peatlands are estimated to hold carbon stocks of 70 Pg C or more as partly decomposed organic matter, or peat. Peat may accumulate over thousands of years into gently mounded deposits called peat domes with a relief of several meters over distances of kilometers. The mounded shapes of tropical peat domes account for much of the carbon storage in these landscapes, but their subtle topographic relief is difficult to measure. As many of the world's tropical peatlands are remote and inaccessible, spaceborne laser altimetry data from missions such as NASA's Global Ecosystem Dynamics Investigation (GEDI) on the International Space Station (ISS) and the Advanced Topographic Laser Altimeter System (ATLAS) instrument on the Ice, Cloud and land Elevation Satellite-2 (ICESat-2) observatory could help to describe these deposits. We evaluate retrieval of ground elevations derived from GEDI waveform data, as well as single-photon data from ATLAS, with reference to an airborne lidar dataset covering an area of over 300 km^2 in the Belait District of Brunei Darussalam on the island of Borneo. Spatial filtering of GEDI L2A version 2, algorithm 1 quality data reduced mean absolute deviations from airborne-lidar-derived ground elevations from 8.35 m to 1.83 m, root-mean-squared error from 15.98 m to 1.97 m, and unbiased root-mean-squared error from 13.62 m to 0.72 m. Similarly, spatial filtering of ATLAS ATL08 version 3 ground photons from strong beams at night reduced mean absolute deviations from 1.51 m to 0.64 m, root-mean-squared error from 3.85 m to 0.77 m, and unbiased root-mean-squared error from 3.54 m to 0.44 m. We conclude that despite sparse ground retrievals, these spaceborne platforms can provide useful data for tropical peatland surface altimetry if postprocessed with a spatial filter.

1. Introduction

The terrain of tropical peatlands is difficult to measure because they can support dense forest canopies (Manuri et al., 2017; Davenport et al., 2020; Honorio Coronado et al., 2021) up to 60 m tall (Anderson, 1983), covering an underlying landscape relief of only meters over horizontal distances of kilometers (Anderson, 1964; Hooijer, 2005; Jaenicke et al., 2008; Cobb et al., 2017; Davenport et al., 2020). This subtle relief arises from the accumulation over thousands of years of partly decayed organic matter, or peat (Richards, 1952), that is typically about 50% carbon by mass (Warren et al., 2012). Thus, the gently convex shape of many tropical peat deposits (Polak, 1933; Anderson, 1964; Lähteenoja et al., 2009) accounts for much of their carbon storage (Cobb et al., 2017; Silvestri et al., 2019; Vernimmen et al., 2020), which amounts to over 70 Gt globally (Page et al., 2011; Draper et al., 2014; Dargie et al., 2017; Warren et al., 2017). Where peatlands have dried out, primarily because of drainage of these deposits for agriculture (Page and Hooijer, 2016), their carbon stores become vulnerable to decomposition and catastrophic fire (Hooijer et al., 2012; Miettinen et al., 2017; Cobb et al.,

* Corresponding author.
E-mail addresses: alex.cobb@smart.mit.edu (A.R. Cobb), rene.dommain@ntu.edu.sg, dommainr@si.edu (R. Dommain), rahayu.sukri@ubd.edu.bn (R.S. Sukri), faizah.metali@ubd.edu.bn (F. Metali), bookhage@uni-potsdam.de (B. Bookhagen), charvey@mit.edu (C.F. Harvey), hao.tang@nus.edu.sg (H. Tang).

https://doi.org/10.1016/j.srs.2022.100074
Received 19 July 2022; Received in revised form 6 December 2022; Accepted 22 December 2022
Available online 26 December 2022

Abbreviations

ATLAS	Advanced Topographic Laser Altimeter System
GEDI	Global Ecosystem Dynamics Investigation
GLAS	Geoscience Laser Altimeter System
ICESat	Ice, Cloud, and land Elevation Satellite
ISS	International Space Station
LP DAAC	Land Processes Distributed Active Archive Center
MAD	Mean absolute deviation
NASA	USA National Aeronautics and Space Administration
RMSE	Root-mean-square error
ubRMSE	Unbiased root-mean-square error

2020). Curbing decomposition and fire by rewetting tropical peatlands (Dohong et al., 2018) could help to meet global climate targets (Leifeld et al., 2019), but requires an understanding of the gradients that drive water flow. Tropical peatland surface gradients tend to be small because peat accumulates where decomposition is retarded by waterlogging, filling in topographic lows and creating a surface topography that is smooth at the landscape scale (Cobb et al., 2017). These surface gradients, however small, control the direction of water flow and also influence many ecological processes in peatlands (Polak, 1933; Anderson, 1964). Thus, maps of the terrain of tropical peatlands are essential for their management and restoration, and also important for understanding their ecology and carbon storage.

Many tropical peatlands are vast and inaccessible (Dargie et al., 2017; Honorio Coronado et al., 2021), and therefore researchers have explored the use of remote sensing approaches to measure their topography, using both airborne (Vernimmen et al., 2019, 2020; Davenport et al., 2020) and spaceborne platforms (Jaenicke et al., 2008; Ballhorn et al., 2009; Berninger and Siegert, 2020). Some peatlands in Southeast Asia are now covered by discrete-return airborne lidar datasets commissioned by governments or private organizations (Vernimmen et al., 2019). Discrete-return airborne lidar datasets are created by laser systems mounted on aircraft typically flying at heights of 500 m–1000 m and emitting tens of thousands to hundreds of thousands of infrared pulses per second (Lim et al., 2003; Liu, 2008). Some of the energy from these pulses is reflected back from ground and canopy surfaces and received by a detector on the aircraft. In discrete-return lidar systems, peaks in the reflected energy that exceed a noise threshold are interpreted as reflections, or "returns", from surfaces on the ground and in the canopy. The geolocation of the reflecting surface is determined with a typical accuracy of about 15 cm vertically and 20–200 cm horizontally based on the travel time of the pulse to and from the surface, and the precise position and orientation of the aircraft-mounted laser (Lim et al., 2003; Liu, 2008). A subset of the geolocated returns is delivered to the client, usually including at least the last return (the lowest surface that reflected enough energy to exceed the threshold), and often including also the first return and up to four returns in between (Lim et al., 2003; Liu, 2008; Mallet and Bretar, 2009).

Deriving a terrain map from discrete-return lidar data requires identifying which returns were reflected from canopy elements or other objects, and which were reflected from the ground. This task, called ground point classification, originally required a substantial amount of manual processing (Sithole and Vosselman, 2004), and therefore became an active area of research. Over the last 20 years, a large number of ground point classification algorithms have been proposed (Sithole and Vosselman, 2004; Roberts et al., 2019). Though they vary in other respects, most algorithms create a model of the ground surface and accept or reject each return as having been reflected from the surface based on spatial information, or "context," in some neighborhood (Sithole and Vosselman, 2004). The most widely applied algorithms use only the inferred x, y, z positions of the reflecting surfaces corresponding to the returns (Axelsson, 2000; Vosselman, 2000; Kraus and Pfeifer, 2001; Zhang et al., 2003, 2016; Evans and Hudak, 2007; Pingel et al., 2013); typically, additional information (such as intensity of the returns, or other remote sensing products) is not used and prior information is provided only through the parameterization of the filter. Many ground point classification algorithms work similarly well on real-world examples (Sithole and Vosselman, 2004; Chen et al., 2013) and digital terrain maps created from airborne lidar with these algorithms are often used as reference terrain maps in peatlands (Jaenicke et al., 2008; Ballhorn et al., 2011; Berninger and Siegert, 2020).

As airborne lidar acquisition is expensive for large areas (Manuri et al., 2017; Vernimmen et al., 2020), coverage is limited, and many existing datasets are not publicly available, lidar from spaceborne platforms has been examined as a source of tropical peatland terrain elevation data in several studies (Ballhorn et al., 2009, 2011; Vernimmen et al., 2020; Berninger and Siegert, 2020). Ballhorn et al. (2009, 2011) explored the measurement of peatland topography using the first operational spaceborne lidar mission, the Geoscience Laser Altimeter System (GLAS) on the Ice, Cloud, and land Elevation (ICESat) satellite. GLAS data products record the amount of energy from each laser pulse that was reflected back to the satellite in elevation intervals of 15 cm near the earth's surface (full waveform data; Harding and Carabajal, 2005; Schutz et al., 2005). Because GLAS data coverage was sparse, with a 172 m along-track spacing between pulses and a track spacing of 29–30 km near the equator (Schutz et al., 2005; Abdalati et al., 2010), many peatlands were hit by very few GLAS pulses, or were missed entirely.

The ongoing Global Ecosystem Dynamics Investigation (GEDI) mission, like GLAS, provides full waveform data, but is designed to provide denser spatial coverage and better penetration of complex tropical forest canopies (Dubayah et al., 2020). GEDI's denser spatial coverage in the tropics arises partly from its orbit on the International Space Station, covering 51.6°S to 51.6°N at a lower altitude than ICESat (419 km vs. 600 km). In addition, GEDI's three lasers have a faster pulse rate (242 Hz vs. 40 Hz) and operate concurrently, with one of these lasers' output split into two beams ("coverage beams; " Dubayah et al., 2020). The coverage beams produce 4.2 mJ pulses, and the full power beams 10.5 mJ pulses, that are dithered to create a total of 8 tracks on the ground and are designed to penetrate extremely dense canopy cover (Wake et al., 2019). The GEDI mission aims to measure canopy structure metrics and above-ground biomass based on profiles of reflected laser energy from the ground to the top of the canopy; the accuracy of these metrics depends on the accuracy of the estimated ground elevation (elev_lowestmode in the GEDI L2A product; Hofton and Blair, 2019) because canopy height metrics are obtained by subtracting the ground elevation from canopy elevations. The accuracy and precision of GEDI L2A geolocation and ground elevation have been evaluated now in a number of studies, including forests and surface waters (Adam et al., 2020; Frappart et al., 2021; Liu et al., 2021; Xiang et al., 2021), although we are not aware of any studies to date exploring its use in tropical peatlands.

The Advanced Topographic Laser Altimeter System (ATLAS), in contrast to GEDI, has primary and secondary missions of measuring changes in polar land and sea ice; nonetheless, ATLAS has a tertiary objective of estimating vegetation biomass (Abdalati et al., 2010), and has been examined as a tool for describing terrain and canopy structure in a number of forested ecosystems (Neuenschwander et al., 2020; Berninger and Siegert, 2020; Davenport et al., 2020; Vernimmen et al., 2020; Xing et al., 2020). Like GEDI, ATLAS provides altimetric data based on the travel time of reflected energy from laser pulses; however, ATLAS produces lower-energy pulses (45 and 175 μJ vs. 4.2 and 10.5 mJ) at a higher frequency (10 kHz vs. 242 Hz) from a higher altitude (~500 km vs. ~419 km) but with a smaller nominal footprint diameter (~11 m vs. ~25 m), and instead of characterizing the reflected energy from the pulse statistically, provides data on individual photons of the laser wavelength received by the detector on the satellite (Neumann

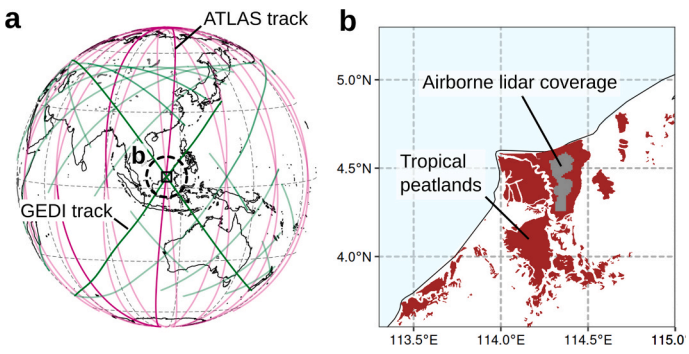

Fig. 1. Study site in Brunei Darussalam. (**a**) Brunei (circled) and several ground tracks for GEDI (green) and ATLAS (fuchsia). (**b**) Site location, showing peatlands (brown) and area with airborne lidar data (gray). (For interpretation of the references to color in this figure legend, the reader is referred to the Web version of this article.)

et al., 2019; Wake et al., 2019; Dubayah et al., 2020; Magruder et al., 2021). ATLAS uses a green (532 nm) laser because of the maturity of photon-sensitive detectors at that wavelength (Neumann et al., 2019), with the tradeoff of a higher background solar irradiance and lower typical reflectance of both canopy and ground elements at this wavelength (Ollinger, 2010) than at the near-infrared (1064 nm) wavelength used in GEDI (Wake et al., 2019) and many airborne lidar systems (Lim et al., 2003; Liu, 2008). Like the GEDI instrument, ATLAS produces multiple beams: in the case of ATLAS, the pulse from a single laser is split by a diffractive optical element into six beams, the stronger of which ("strong beams") have an energy per pulse about 4 times that of the weaker beams ("weak beams"; Neumann et al., 2019). ATLAS data products provide geolocated photons (in data product ATL03), instead of waveforms or peaks, with a higher-level product (ATL08) that classifies photons as ground or canopy using a clustering algorithm called Differential, Regressive and Gaussian Adaptive Nearest-Neighbor, or DRAGANN (Neuenschwander and Pitts, 2019).

Several recent studies have explored ATLAS as a tool for characterizing tropical peatland terrain and canopy structure (Berninger and Siegert, 2020; Davenport et al., 2020; Vernimmen et al., 2020), and showed that the dense canopy in some tropical peatlands can be problematic, as it may, in places, prevent the sensor from receiving any photons reflected from the ground (Berninger and Siegert, 2020; Davenport et al., 2020). These studies were able to obtain tropical peatland terrain data from ATLAS by focusing on degraded areas with thinner canopies and forest gaps, but there are still vast peatland areas that are covered with dense vegetation, especially in the less-described peatlands of New Guinea (Bleeker, 1983), the Congo (Évrard, 1968; Dargie et al., 2017), and the Amazon (Lähteenoja et al., 2009; Hastie et al., 2022).

In this study, we compare GEDI and ATLAS data to an airborne lidar dataset covering an area of over 300 km^2 of forested tropical peatland in the Belait District of Brunei Darussalam. We first examine the full waveform data from the GEDI L1B product and geolocated bounce point data from the ATLAS ATL03 product to illustrate the general agreement between these and the reference discrete-return airborne lidar data. We then evaluate ground elevations from the GEDI L2A dataset and ATLAS ATL08 dataset with reference to ground returns from airborne lidar in the neighborhood of each GEDI or ATLAS shot. Because of dense forest cover—differing from previous studies but similar to the less-explored peatlands of the tropics—we find that standard GEDI and ATLAS products in our study area often place the ground elevation within the canopy. We therefore explore whether GEDI and ATLAS can nonetheless provide useful terrain elevations in tropical peatlands with a dense canopy, if the data are postprocessed with a spatial filter.

2. Materials and methods

We first describe the vegetation and terrain in the study area, and outline the pre-processing of the three datasets: airborne lidar, GEDI and ATLAS. Next, we present our methods for spatial filtering of GEDI and ATLAS ground elevations, and how the results were evaluated with reference to airborne lidar.

2.1. Study site

The study area lies in the Belait district of Brunei Darussalam, on the northwest coast of Borneo (Fig. 1). Vegetation consists primarily of intact, closed-canopy peat forest (Fig. 2) dissected by tributaries to the Belait River, with a few cleared areas from discontinued logging concessions, and a naturally open, savanna-like vegetation type referred to as padang keruntum (after a local name for the dominant tree, *Combretocarpus rotundatus*) in the southwest corner of the study area. In the forested areas, the canopy is multilayered, with a continuous or

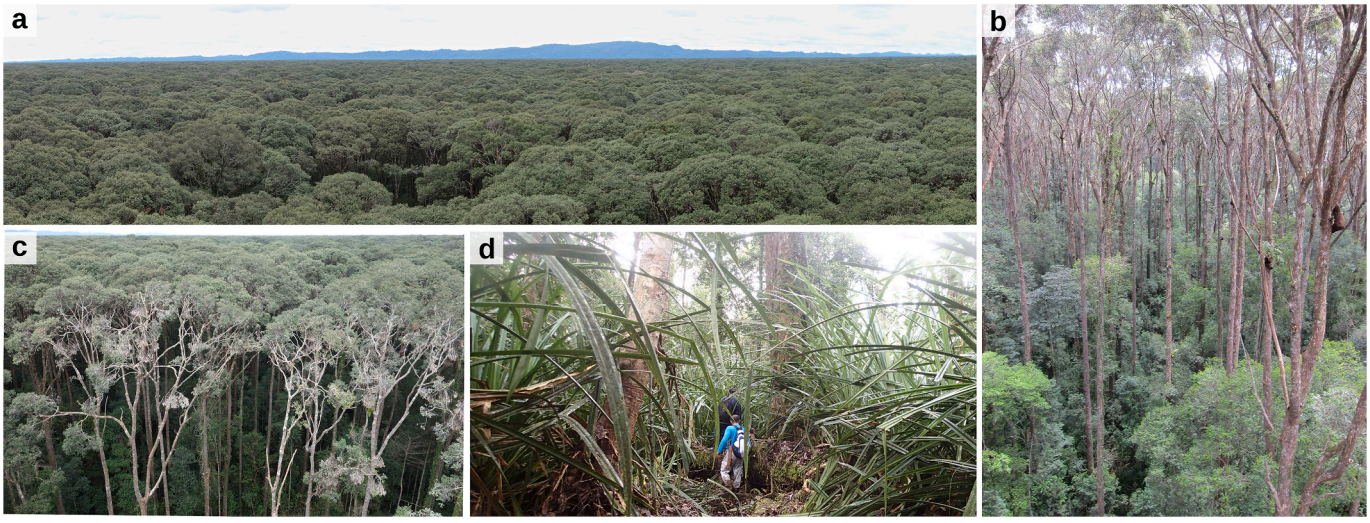

Fig. 2. Forest cover in the study area. (**a**–**c**) Undisturbed forest within the area of full point cloud data, from above (a, c) and just below (b) the 50 m-high canopy. (**d**) Surface microtopography created by buttresses, giant rhizomes and partly decayed organic matter.

discontinuous upper canopy that is in most places dominated by the tall dipterocarp tree *Shorea albida*, a lower canopy comprising a range of other tree species, and a dense understory of giant herbs and saplings. The underlying terrain is characterized by small surface gradients of about 1 m/km, on which is superposed a complex microtopography with a relief of about 30–50 cm created by buttresses, giant rhizomes and partly decayed organic matter (Fig. 2).

The vegetation types of peatlands in northwest Borneo were described by Anderson (1961, 1963, 1964) based on sample plots and transects throughout Brunei and adjacent Sarawak (Malaysia). In the savannah-like padang keruntum vegetation type, Anderson (1961) observed an average of 297 trees ha^{-1}, with the largest trees 12.2–15.2 m tall, and an average tree basal area of 8.3 m^2 ha^{-1}. In the closed-canopy vegetation types (excluding the *Tristania-Parastemon* association, which occupies a narrow transition zone around padang keruntum), Anderson (1961) observed an overall canopy height range of 27.4–57.9 m, with averages of forest density by forest type ranging 504–756 trees ha^{-1} and average basal area ranging from 33.5 to 49.6 m^2 ha^{-1}. We have not found any studies of canopy cover in these forest types preceding the airborne lidar analysis conducted here (section 2.2.1).

2.2. Datasets and pre-processing

We describe here the processing of airborne lidar, and the pre-processing and subsetting of GEDI and ATLAS data. We include in this section the classification of airborne lidar ground returns, because this application of spatial filters is well established. In contrast, application of spatial filters to GEDI and ATLAS data is the purpose of this study, and is therefore described in subsection 2.3 (Methods).

2.2.1. Airborne lidar data

Airborne lidar data were obtained from the Brunei Survey Department as 1 km × 1 km tiles produced by TerraScan software in LAS format version 1. Data were collected in 2009 and early 2010 by an Optech Gemini system on a NOMAD airplane. The system emitted near-infrared (1064 nm) laser pulses at 100 kHz from a height of 1400 m, producing an estimated 28 cm beam width on the ground. The laser was swept through a scan angle of ±22° at 40 Hz, producing a swath width of 1131 m and line spacing of 792 m (swath overlap 30%).

The LAS airborne lidar data tiles provided by the Brunei Survey Department starting in 2010 included up to four returns (first, last, and two intermediate). Later, data were provided in two data products classified using an undisclosed method, with either a subset of the last returns or of the first returns for each tile. We obtained full point clouds (up to four returns) for 78.8 km^2, the subsets of first and last returns for an additional 48.3 km^2, and the subsets of last returns only for an additional 194.3 km^2, for a total of 321.4 km^2. Because the first- and last-return tiles only contained data from a subset of pulses, we estimated the pulse density from the LAS tiles with full point cloud data (up to four returns), as the total number of last returns reported in the LAS files divided by their total area.

To classify ground returns within the airborne lidar data, we used the progressive morphological filter (PMF) of Zhang et al. (2003) as implemented in an open-source software package (the Point Data Abstraction Library, PDAL; https://pdal.io/). This algorithm uses progressively larger windows, performing an erosion (mathematical morphology) operation at each scale and discarding points lying more than a threshold above the eroded surface. At each window size, points that lie above the eroded surface by a distance of more than max_distance, or more than window_size × slope + initial_distance, are considered non-ground points. The roles of these parameters are therefore as follows: the initial_distance threshold constrains the allowable relief at even the smallest scales, while the slope constrains the relief to a range that increases with the window size. The maximum window size determines the horizontal distance beyond which the constraint imposed by the slope parameter should no longer apply, and max_distance sets an absolute limit on the relief allowed at any window size. In practice, we were able to find a reasonable parameterization for ground point classification in the airborne lidar data with little experimentation based on prior knowledge of the microtopographic relief and typical large-scale gradients at the site. We set initial_distance, slope and max_distance to 15 cm, 0.02 and 2.5 m, respectively, and set the maximum window size to 200 m.

To describe the extent to which dense vegetation prevented laser energy from reaching the ground, we defined ground visibility from the perspective of the airborne lidar system as the number of true ground returns divided by the total number of pulses, and estimated ground visibility as the density of last returns classified as ground by the spatial filter, divided by the mean density of impulses in the area with full point cloud data. In making this approximation, we assumed that the Survey Department processing of the last-return "DTM" datasets did not remove many true ground points (small omission error), which is consistent with the occurrence of non-ground last returns in these files (commission errors), as there is usually a tradeoff between omission and commission errors in ground point classification algorithms (Sithole and Vosselman, 2004). We use "ground visibility" to emphasize that we do not assume or estimate a precise relationship between this commonly used quantity (Lovell et al., 2003) and gap fraction (nadir-projected gap area divided by total area) or its complement, canopy cover, because this relationship depends on: (1) the ratio of backscattering coefficients of vegetation and ground elements (Ni-Meister et al., 2001; Harding et al., 2001); (2) the distribution of energy in returns from ground and vegetation, which does not have a well defined link to the "intensity" reported in airborne lidar data (Mallet and Bretar, 2009; Armston et al., 2013); and (3) the distribution of gap sizes relative to the width of the diffraction cone of the beam from the aircraft, which affects whether reflected energy from ground or vegetation is intense enough to generate a "return" via the lidar system's proprietary triggering mechanism (Mallet and Bretar, 2009; Armston et al., 2013).

2.2.2. Spaceborne lidar data: GEDI/ISS

We obtained all available GEDI L1B and L2A Version 2 data between 4.226 and 4.621°N, 114.246 and 114.450°E, from NASA's Land Processes Distributed Active Archive Center (LP DAAC; Dubayah et al., 2022a,b) from the beginning of the mission through June 29th, 2022. To illustrate the GEDI tracks intersecting the study area (Fig. 1), we also obtained granule metadata (NASA Earthdata portal, https://earthdata.nasa.gov/) for a northwest-southeast track from orbit 2973, and adjacent orbits (2969–2975); and for a southwest-northeast track from orbit 3073, and adjacent orbits (3069–3076).

To evaluate GEDI terrain data, we extracted GEDI ground elevation estimates from GEDI L2A data. GEDI L2A version 2 provides several different ground point estimates for each shot, obtained by smoothing the received waveform with a Gaussian filter and identifying peaks that exceed a threshold: there are 6 different parameterizations ("algorithms") used for waveform processing in the L2A product, which differ in the width of the Gaussian filter (smoothwidth_zcross) and the thresholds used to identify the top of the canopy (front_threshold) and the ground (back_threshold; Hofton and Blair, 2019, Table 1). Algorithms 1 and 4 use the widest smoothing kernel and the highest threshold for ground detection, and are therefore the least likely to mistake noise at the end of the waveform for a ground reflection, but the most likely to miss a weak ground signal. Algorithms 1 and 4 have identical parameters for ground detection, and therefore provide very similar sets of ground points, but may flag different shots as valid (quality_flag) because of different values for the parameter that identifies the top of the canopy (front_threshold). Algorithms 2, 3, 5 and 6 all use the same kernel width, which is about 0.54 times the width used for algorithms 1 and 4. Among these, the threshold for ground detection decreases (and sensitivity increases) in the order 3, 6, 2, 5, where 3 has a threshold equal to algorithms 1 and 4 (but with a narrower smoothing

Table 1
GEDI waveform processing algorithm parameter sets, after Hofton and Blair (2019). The parameter smoothwidth, equal to 6.5 for all algorithms, is not shown.

Algorithm	smoothwidth_zcross[a]	front_threshold[b]	back_threshold[c]
1	6.5	3σ[d]	6σ
2	3.5	3σ	3σ
3	3.5	3σ	6σ
4	6.5	6σ	6σ
5	3.5	3σ	2σ
6	3.5	3σ	4σ

[a] Width of Gaussian filter used to search signal-only portion of waveform for peaks.
[b] Threshold above mean noise level for first (highest-elevation) peak.
[c] Threshold above mean noise level for last (lowest-elevation) peak.
[d] σ: noise standard deviation after initial smoothing.

Table 2
Parameterizations of progressive morphological filter of Zhang et al. (2003).

Application	max_distance	initial_distance	slope	max_window_size
Airborne lidar[a]	2.5 m	15 cm	0.02	200 m
GEDI[b,c]	12 m	15 cm	0.0012	10 km
ATLAS[b,c]	12 m	15 cm	0.0012	1 km

[a] Application to airborne lidar is a standard use for this type of filter; parameterization is shown for reference.
[b] Applied in one horizontal dimension along each flight transect.
[c] To explore sensitivity to these parameters, four additional parameterizations were generated for this filter by increasing each parameter by 10%, one at a time.

kernel; Hofton and Blair, 2019, Table 1).

In addition to the ground estimate obtained from each of these algorithms as the lowest detected mode (elev_lowestmode), GEDI L2A also stores a "selected" ground estimate, which is equal to a mode from one of the 6 waveform processing parameterizations, but not necessarily the lowest mode (Hofton and Blair, 2019). We analyzed the set of "selected" ground estimates separately because (1) the "selected" algorithm may differ for different shots, and therefore the set of "selected" ground elevations is a mixture of modes from the 6 waveform processing algorithms; and (2) the "selected" mode for a shot may not be the lowest mode of the "selected" algorithm, and therefore may not be equal to any of the 6 other ground elevations for the shot. We extracted all points flagged as viable for downstream use (quality_flag = 1; Hofton and Blair, 2019) from each of these sets of ground points.

2.2.3. Spaceborne lidar data: ATLAS/ICESat-2

We obtained all available ATLAS/ICESat-2 L2A Global Geolocated Photon Data (ATL03) and L3A Land and Vegetation Height (ATL08) Version 5 data from LP DAAC (Neuenschwander et al., 2022a; Neumann et al., 2022) for the same spatial region as for GEDI data from the beginning of the mission through June 29th, 2022. ATL03 provides the geolocation of the bounce point of each photon at the ATLAS laser wavelength received by the ATLAS telescope. We filtered geolocated photon bounce points based on their classification as signal in the ATL08 product (classed_pc_flag 1, 2, or 3; Neuenschwander et al., 2022b). Because the name attached to each of the six ATLAS beams (GT1L, GT1R, …) depends on the spacecraft orientation (Neuenschwander et al., 2022b), we used spacecraft orientation (sc_orient) to determine the names for weak and strong beams in each transit. To illustrate the ATLAS tracks intersecting the study area (Fig. 1), we also obtained Reference Ground Tracks (RGTs) with dates and times as KML from the ATLAS specifications page (https://icesat-2.gsfc.nasa.gov/science/specs).

2.3. Methods

We now describe the spatial filtering of GEDI and ATLAS data, and the alignment and comparison of GEDI, ATLAS and airborne lidar datasets. Because the flight paths of the ISS and ICESat-2 intersect one another obliquely, we did not attempt to compare the GEDI and ATLAS datasets directly. Instead, we evaluated GEDI and ATLAS elevations with reference to the airborne lidar dataset, which provides ground elevations throughout the study area.

2.3.1. Spatial filtering of GEDI data

To simplify further analysis, we first defined a transect for each beam and each pass of the GEDI instrument over the study area, by orthogonal distance regression of the set of georeferenced beginning and end points (bin0 and lastbin) from all GEDI waveforms in the transect. To explore the use of spatial filters for removing outliers, we processed GEDI ground elevations using the same type of spatial filter used for the airborne lidar data (PMF, in PDAL), using, as input to the filter, the elevation and along-track position of the interpolated ground point. We selected parameters for the spatial filter based on typical surface gradients in the study area and the spatial configuration of the GEDI shots, followed by a few rounds of trial-and-error in which we examined profiles of classified GEDI ground points without reference to the airborne lidar data. We arrived at parameters of 12 m, 0.0012, 15 cm, and 10 km for max_distance, slope, initial_distance, and max_window_size, respectively (Table 2).

Because in some important applications one would not have access to a reference airborne lidar dataset, we did not attempt to optimize the parameters for filtering GEDI data. Instead, to explore the sensitivity of GEDI ground point classification to the filter parameters, we perturbed the four filter parameters by separately increasing each of them by 10%. We then computed all error metrics (see section 2.3.4 for the error metrics calculated) for all 5 parameter sets: the initial parameterization (Table 2), and the four perturbed parameter sets produced by increasing each parameter by 10%, one at a time.

2.3.2. Spatial filtering of ATLAS data

As with GEDI, to simplify further analysis, we first defined a transect associated with each pass of each beam of the ATLAS instrument over the study area by orthogonal distance regression of the ATL03 reference photons associated with the transect. We extracted geolocations of ATL03 photon bounce points classified as ground by the DRAGANN algorithm in ATL08 (Neuenschwander and Pitts, 2019). To explore the use of spatial filters to identify bounce points misclassified as ground in ATL08, we processed the ATL08 ground photons using the same spatial filter used for the airborne lidar and GEDI data (PMF, in PDAL), using, as input to the filter, the elevation and along-track position of the photon bounce point. We used the same spatial filter parameters for ATL08-classified ground points as for geolocated GEDI ground elevations (section 2.3.1, "Spatial filtering of GEDI data"), but with a smaller max_window_size of 1 km (Table 2) due to the higher density of candidate ground points per distance provided by ATL08 ground photons compared to GEDI shots. As with the filtering of GEDI ground points, we explored sensitivity to these parameters for spatial filtering of ATL08 ground photons by separately increasing each parameter by 10%, and computing error metrics for each parameter set, yielding 5 sets of error metrics (section 2.3.5).

2.3.3. Alignment of datasets

The typical geolocation error of airborne lidar systems is <2 m (Lim et al., 2003; Liu, 2008). On-orbit evaluation has shown geolocation error for all ATLAS beams to be in the range of 2.5–4.4 m (mean + 1σ; Luthcke et al., 2021), while GEDI geolocation error is estimated to be 10–20 m (Dubayah et al., 2020). Although a number of previous studies have added a horizontal offset to spaceborne lidar geolocations to maximize agreement between spaceborne and airborne lidar vegetation profiles

(Harding and Carabajal, 2005; Popescu et al., 2011; Neuenschwander et al., 2020a), we did not perform this step because the small gradients in surface elevation in the study area (about 1 m/km) would combine with GEDI and ATLAS geolocation error to produce elevation errors of <2 cm.

2.3.4. Data comparison: GEDI vs. airborne lidar

To compare GEDI waveforms and ground elevation data to airborne lidar data, we extracted airborne lidar returns within the neighborhood of GEDI transects (workflow shown in Fig. 3). We first pre-filtered airborne lidar tiles by extracting data within 18 m of the bounding box of the intersecting transect, then performed a spatial query (using PostGIS, https://postgis.net/) to obtain only returns within 18 m of the transect center line. These 36 m-wide strips of airborne lidar returns were used in subsequent analyses to reduce the computing time for spatial searches within the ~25 m-diameter footprint (Dubayah et al., 2020) of each GEDI shot without omitting relevant data due to deviation of individual shots from the transect center line.

To qualitatively compare GEDI waveforms to discrete-return airborne lidar data within the study area, we constructed pseudowaveforms, or vertical distributions of returns (Blair and Hofton, 1999), from airborne lidar returns within each GEDI shot in the area of full (up to four return) airborne lidar data. To extract airborne lidar returns within a GEDI shot, we queried the airborne lidar returns to obtain only those within the shot radius of 12.5 m of the slanted central axis of the GEDI shot. We then constructed a pseudowaveform as the distribution of elevations of airborne lidar returns within the GEDI shot. We did not weight returns by distance from the central axis of the GEDI shot because weighting was found to make little qualitative difference in a similar analysis of GLAS data (Popescu et al., 2011), and our primary focus was on ground elevations.

To quantify the agreement between GEDI and airborne lidar terrain data, we also compared each GEDI ground elevation to the mean elevation of airborne lidar ground returns within the GEDI shot. We were able to perform this comparison in all areas with airborne lidar coverage, as all airborne lidar data included last returns classified as ground using the spatial filter (section 2.2.1, "Airborne lidar data"). For each set of GEDI ground elevations, we compared each GEDI ground point to the mean airborne lidar ground elevation within each shot in terms of bias (difference in mean), root mean squared error (RMSE), and mean absolute difference (MAD). Because we are also interested in how the overall shape of the peat surface estimated from GEDI corresponds to the shape of the reference surface from airborne lidar data, we also computed the unbiased root-mean-squared error (ubRMSE), defined as the root-mean-squared difference between the deviations of GEDI and of airborne lidar ground elevations from their respective means along each transect. We evaluated these metrics for all ground elevations in the GEDI L2A product, and also for ground points that passed the spatial filter. Finally, to explore sensitivity of these results to filter parameters, we then recalculated all metrics for four sets of perturbed parameters generated by separately increasing each filter parameter by 10% (section 2.3.1).

2.3.5. Data comparison: ATLAS vs. airborne lidar

To compare ATLAS photon data and ground elevations to reference airborne lidar data, we extracted airborne lidar returns within the neighborhood of ATLAS transects using the same approach as for GEDI transects (workflow shown in Fig. 3), but with narrower (17 m-wide) strips of airborne lidar due to the smaller diameter of the ATLAS footprint (~11 m; Magruder et al., 2021).

To compare the vertical distribution of nadir-visible reflectors detected in ATLAS geolocated photon data and from airborne lidar data, we used a similar approach as for GEDI waveforms (section 2.3.4) but additionally needed to construct pseudowaveforms from ATLAS photon bounce points as follows. We divided the data from each transit of the ATLAS instrument over areas with full point cloud airborne lidar data (up to four returns) into 200 m along-track segments. We then constructed pseudowaveforms from the distribution of ATL03 photon bounce point elevations within the segment, which we compared to the distribution of airborne lidar return elevations within the beam radius (5.5 m) of the center line along each segment. As with the comparison to GEDI waveforms, we performed no weighting of airborne lidar returns by distance from the transect center line.

To quantify the agreement between ATLAS and airborne lidar terrain data, we compared ATL08 and airborne lidar ground elevations using the same approach as for evaluation of GEDI ground points (section 2.3.4), with the sole difference being the radius used to identify airborne lidar ground returns within the shot footprint (5.5 m for ATLAS vs. 12.5 m for GEDI).

3. Results

3.1. Ground visibility to airborne lidar

Filtered airborne lidar data provided a reference digital terrain map that was free from outliers caused by false ground returns: because the total relief of the study site is only 16.7 m, outliers from the 30–50 m canopy would be immediately visible in a shaded relief image (Fig. 4a). However, airborne lidar data also revealed that average ground visibility in the study area was low: data from the area with full point cloud data (up to four returns) indicated a pulse density of 1.945 m^{-2}, whereas the density of ground-classified returns in the study area was 0.0550 m^{-2}, for a mean ground visibility of 2.83%. Overall, 87.6% of the study area had a ground visibility of less than 5% and 47.8% had a ground

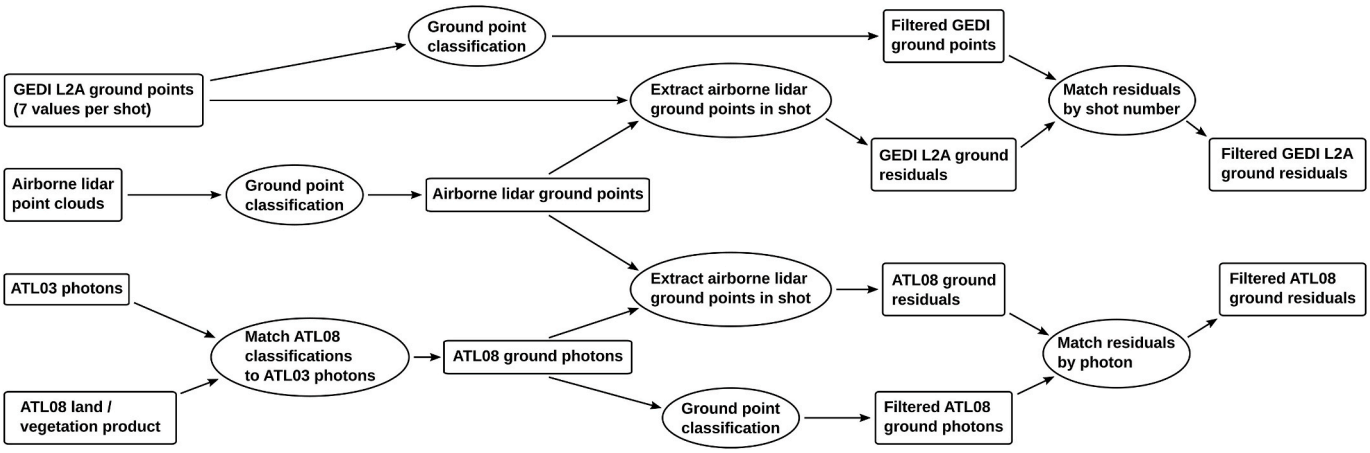

Fig. 3. Flow chart for GEDI, ATLAS and airborne lidar data processing.

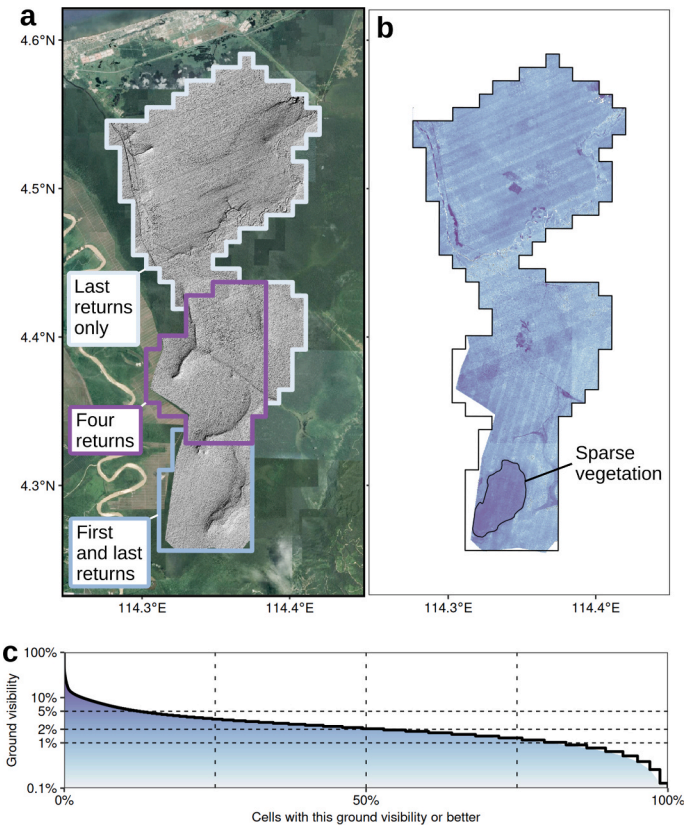

Fig. 4. Airborne lidar coverage and ground visibility in the study area. (**a**) Shaded relief map of study area derived from airborne lidar (resolution 20 m × 20 m), showing areas with point cloud data (4 returns), first and last returns, and last returns only. Total relief is 16.7 m. (**b**, **c**) Ground visibility in the study area, defined as the ratio of returns classified as ground to the pulse density; note logarithmic color scale. The demarcated area has naturally sparse vegetation (padang keruntum; Anderson, 1963). (For interpretation of the references to color in this figure legend, the reader is referred to the Web version of this article.)

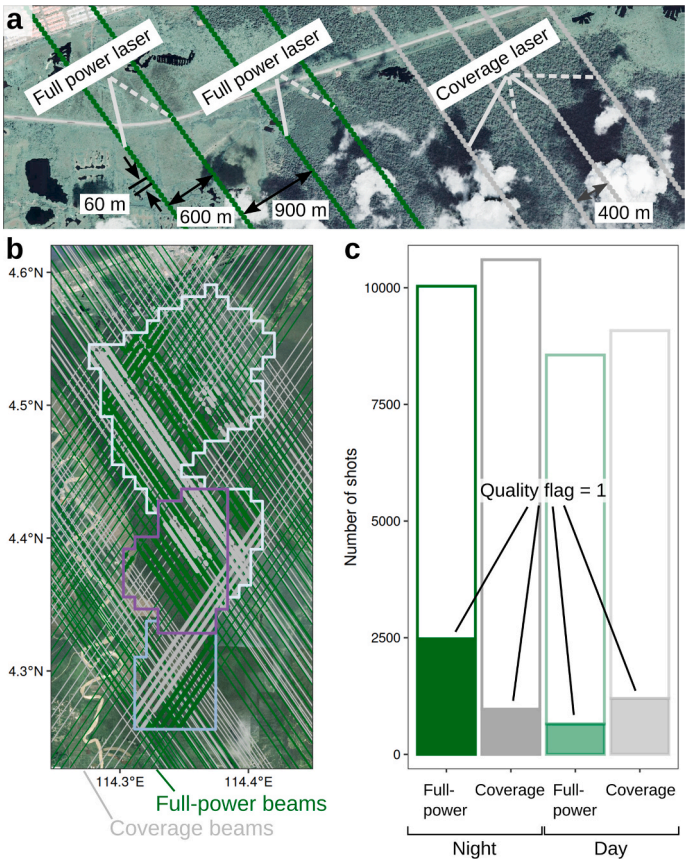

Fig. 5. GEDI coverage of the study area. (**a**) Beam configuration of GEDI. Shots from GEDI full power and coverage lasers from a single transit by the ISS and (**b**) GEDI transects over the study area from full power (green) and coverage beams (gray). Shots marked as valid for downstream use (quality_flag = 1, "selected" algorithm) in the GEDI L2A product are shown as points (small points: night; smaller points: day). (**c**) Number of GEDI shots from full power and coverage beams in the area of airborne lidar data; filled portions indicate quality-filtered shots from the "selected" algorithm of the GEDI L2A product (shots flagged as valid differ somewhat across algorithms). (For interpretation of the references to color in this figure legend, the reader is referred to the Web version of this article.)

visibility of less than 2% (Fig. 4b and c). Ground visibility was much higher in the sparsely vegetated (padang keruntum) area, with an average of three times more ground-classified returns per area (0.1741 m^{-2}; mean ground visibility 8.95%). Only 5.04% of the sparsely vegetated area had a ground visibility of less than 5% and only 0.11% had a ground visibility of less than 2%.

3.2. Spaceborne lidar data: GEDI/ISS

The study area was crossed by 23 passes of the GEDI instrument; across all 8 beams, the study area was intersected by 170 distinct transects, covering a total linear distance of 1099 km by coverage beams and 1037 km by full-power beams (Fig. 5). There were 38,275 GEDI shots in the study area described in the GEDI L1B product, of which 20,634 were at night (54%). In all, 5292 shots (14%) were flagged as suitable for further analysis (quality_flag = 1) using the "selected" algorithm, 65% of them at night (Fig. 5c). Based on the distance traversed, the linear density of quality shots at night was 1.52 shots km^{-1} from the coverage beams and 4.11 shots km^{-1} from the full-power beams. There was good qualitative agreement between GEDI waveforms and airborne lidar returns where full point cloud airborne lidar data were available, as evident in cross-sections (Figs. 6 and 7). Nonetheless, the lowest mode of the GEDI waveforms often appeared somewhat higher than the mean elevation of ground-classified airborne lidar returns (Fig. 6).

Profiles of GEDI ground elevations with airborne lidar data in densely forested areas showed that ground elevations selected in the GEDI L2A product included a number of high outliers (Fig. 8), even under the best conditions (passing quality flags, sensitivity ≥98%, full-power beam at night). These high outliers occurred when the GEDI L2A ground elevation was placed within the canopy in areas of dense forest cover. Most or all of these canopy "ground" elevations were removed by the spatial filter, depending on which GEDI L2A algorithm was used to determine the ground elevation for each shot (see below). The filtered GEDI L2A-selected ground elevations lay near, but mostly above, the elevation of the airborne lidar ground returns (Figs. 8, 9a and 9b).

For all GEDI L2A algorithm settings, ground elevations that passed the spatial filter were more accurate and precise than unfiltered ground elevations, including shots with a sensitivity of over 98%, according to all error metrics (bias, RMSE, ubRMSE and MAD) and all algorithms

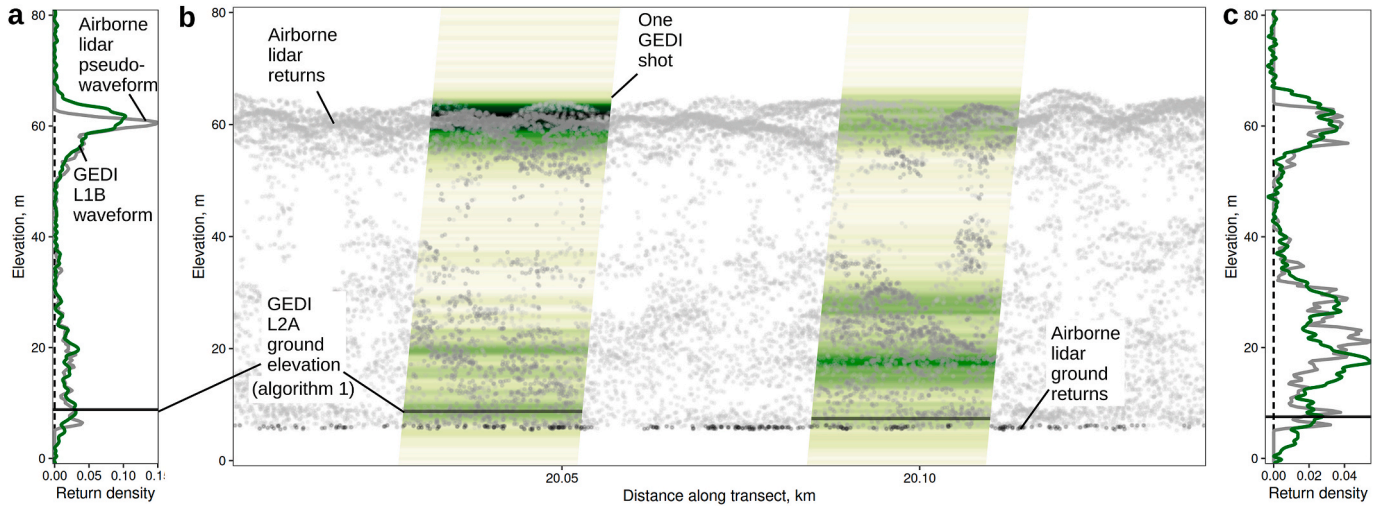

Fig. 6. Sample GEDI waveforms and corresponding airborne lidar pseudowaveforms. (**a, c**) GEDI waveforms (green) from two shots at night from a full-power beam and pseudowaveforms constructed from airborne lidar point cloud data (gray) using a kernel density estimator; black horizontal lines show the elevation of the waveform mode identified as ground by GEDI L2A algorithm 1. (**b**) Profile of GEDI beams and of the airborne lidar returns used to construct the pseudowaveforms (a, c), shown with nominal beam width of 25 m. (For interpretation of the references to color in this figure legend, the reader is referred to the Web version of this article.)

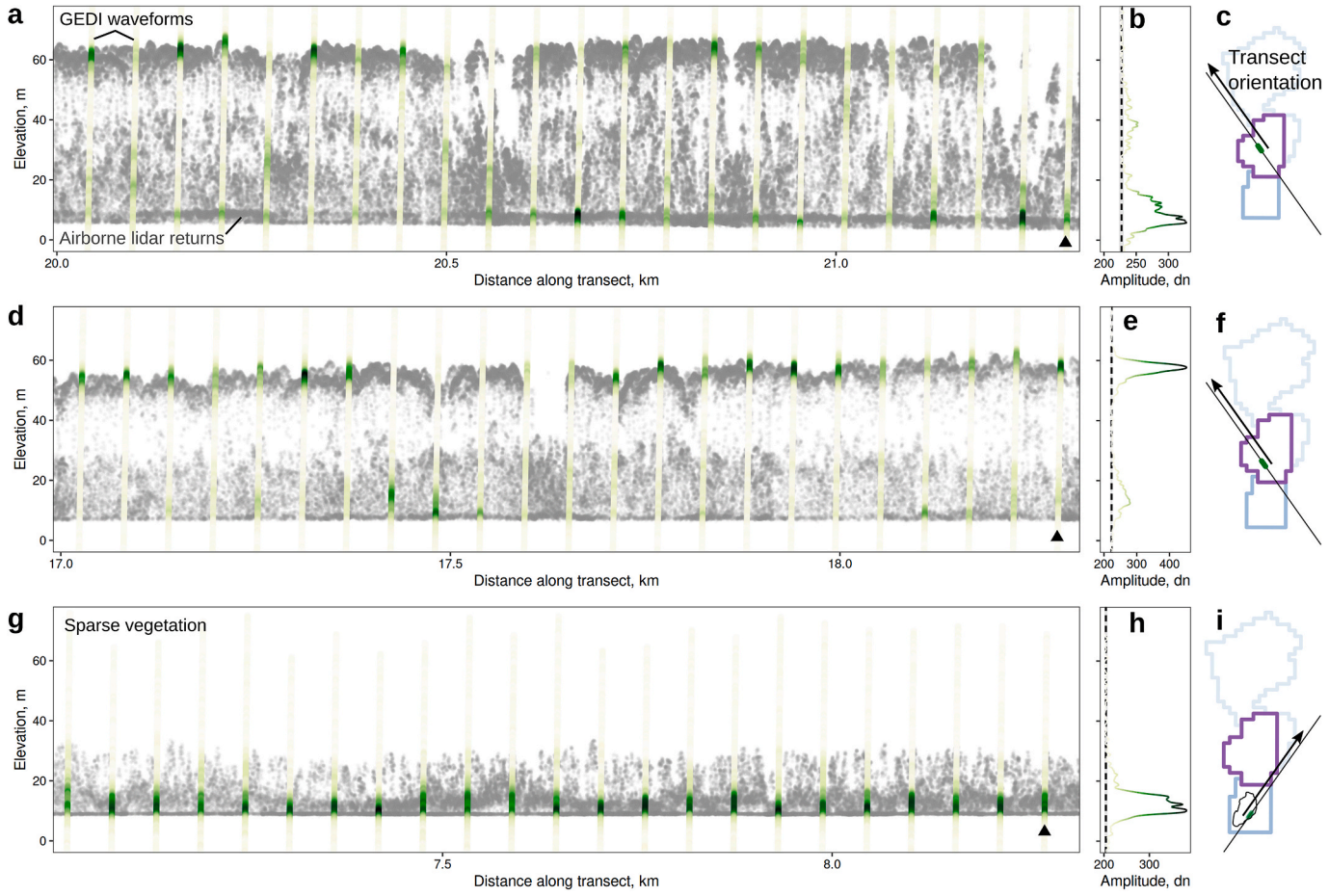

Fig. 7. Profiles of GEDI waveforms (green; full power beams at night) and airborne lidar (gray). (**a, d, g**) Airborne lidar returns within 18 m of the GEDI transect center line (gray) and GEDI L1B waveform data (shades of green). (**b, e, h**) Sample GEDI waveforms (marked with triangles in a, d, g) from along each transect, as uncalibrated signal amplitudes (digital number, dn). Dashed line and shaded bands show estimated noise level and standard deviation from the GEDI L1B product. (**c, f, i**) Locations of profiles (a, d, g) in study area. (For interpretation of the references to color in this figure legend, the reader is referred to the Web version of this article.)

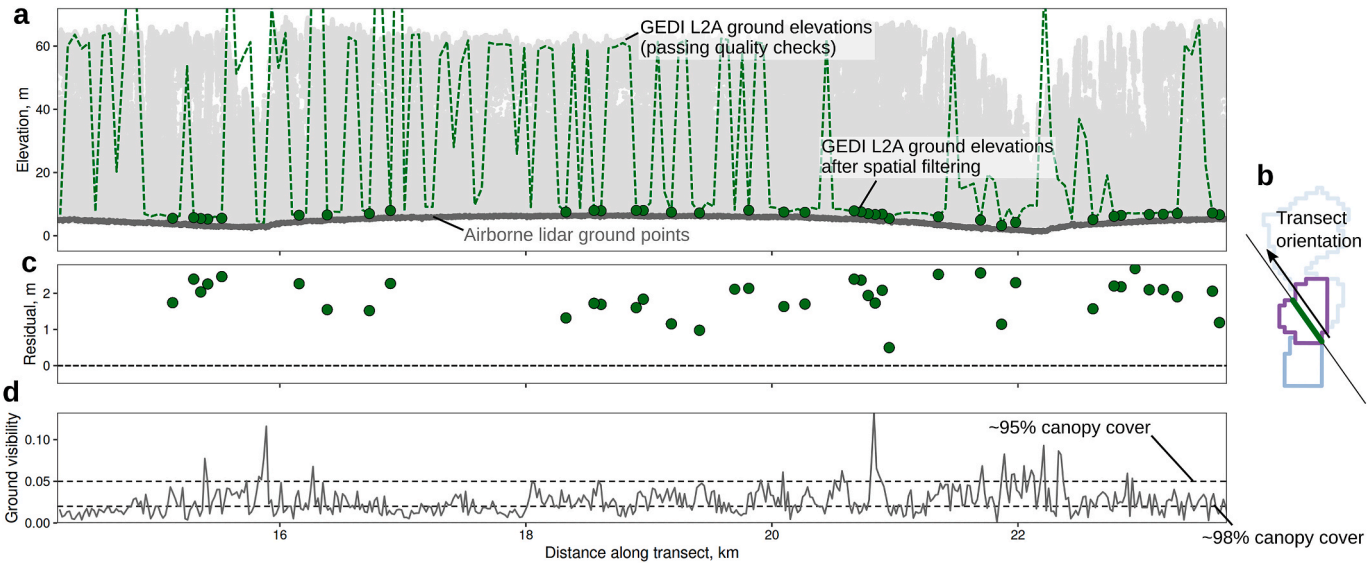

Fig. 8. GEDI ground elevations. (**a**) GEDI L2A ground elevations before (algorithm 1; green dashed line) and after spatial filtering (points), and airborne lidar ground returns (gray). (**b**) Location of transect shown in (a, c, d). (**c**) Difference between spatially filtered GEDI L2A ground elevation and average elevation of airborne lidar ground returns within the same GEDI shot. (**d**) Ground visibility estimated from airborne lidar data along the transect. (For interpretation of the references to color in this figure legend, the reader is referred to the Web version of this article.)

(Fig. 9c–e) except for a larger bias with spatial than with sensitivity filtering for algorithm 5 (Fig. 9e). For those algorithms that identified some shots in the study area as having sensitivities of over 98%, the distribution of residuals for those high-sensitivity shots was similar to the overall distribution of residuals of ground elevations determined by that algorithm (Fig. 9c). With algorithms 2, 3, 5, and 6, some positive outliers remained in the filtered ground points, whereas in algorithms 1 and 4 the spatial filter appeared to remove all non-ground outliers. Ground points from algorithms 1 and 4 were identical except that two shots were flagged as viable by algorithm 4 but not by algorithm 1 (3344 vs. 3342 quality shots), and because of this difference, one less point passed the spatial filter in the algorithm 4 point set (1153 vs. 1154; results in Fig. 9 plots were visually indistinguishable).

Algorithms 2, 3, 6 and especially 5 additionally included some large negative outliers, which cannot be removed by the spatial filter we used; there were also some negative outliers among the ground elevations selected in the GEDI L2A product, attributable to the selection of algorithm 5 for some shots. Nonetheless, error metrics of ground points from the entire study area that passed the spatial filter approached, and in most cases improved on, the accuracy and precision of ground points from quality GEDI shots in the sparsely vegetated southwest corner of the study area. For example, GEDI L2A ground points from algorithm 1 in the sparsely vegetated area, alone, had much better error metrics than the complete set of ground points, with a vertical offset (bias) of 3.08 vs. 8.35 m, a MAD of 3.08 vs. 8.35 m (bias and MAD were nearly equal for these point sets), a RMSE of 3.86 vs. 15.98 m, and a ubRMSE of 2.32 vs. 13.62 m. However, the 1154 out of 3342 ground points from the entire study area that passed the spatial filter had still better error metrics, with a bias and MAD, RMSE, and ubRMSE of 1.83, 1.97, and 0.72 m, respectively: 4.6, 8.1 and 19 times better than the metrics for unfiltered ground points (Fig. 9d and e).

3.3. *Spaceborne lidar data: ATLAS/ICESat-2*

The study area was crossed by 12 passes of the ATLAS instrument; across all 6 beams, the study area was intersected by 37 distinct transects, covering a total linear distance of 302 km by weak beams and 334 km by strong beams (Fig. 10). From these transects, there were 3,593,941 photons received by ATLAS and described in the ATL03 product as having bounce points in the study area, of which 73,575 were received at night (2.27%). In all, 112,800 of the received photons (3.14%) were classified as signal in the ATL08 product, 51.0% of them at night (Fig. 10c). Based on the distance traversed, the linear density of ATL08-classified signal photons was 41.4 photons km^{-1} from the weak beams and 300.6 photons km^{-1} from the strong beams.

Point cloud data from ATL03 bounce points and airborne lidar returns appeared qualitatively similar in cross-sections (Figs. 11 and 12). Pseudowaveforms produced from ATL03 photon bounce points and airborne lidar returns were also qualitatively similar, though the airborne lidar canopy profiles were more detailed (Fig. 11a and c) because of the higher density of airborne lidar returns (1.945 returns m^{-2} in airborne lidar vs. 0.106 ATL08 signal photons m^{-2} from strong beams at night). In areas of dense forest cover, profiles showed that there were intervals of more than 50 m in which none of the ATLAS photon bounce points were on the ground (Fig. 12).

Photon bounce points classified as ground in ATL08 were not always on the ground; some were close to the ground but above it (Fig. 11), others were within the forest canopy (Fig. 13). The daytime ATLAS shots did not seem to produce any useful data (data not shown); however, both strong and weak beams at night yielded good ground elevations (Fig. 14). Similar to the GEDI L2A ground elevations, residual plots showed that the mode of ATL08 nighttime ground photon bounce points lay above the reference ground surface derived from airborne lidar (Fig. 14b); in addition, and in contrast to the ground elevations from some GEDI L2A algorithms, almost all ATL08 ground elevations lay at or above the mean elevation of airborne lidar ground points within the ATLAS shot (Figs. 13c and 14). As with GEDI L2A ground elevations, the spatial filter effectively removed the canopy photons misclassified as ground in ATL08 nighttime data (Figs. 13 and 14), resulting in error metrics that were close to those of unfiltered ATL08 ground points in the area of sparse vegetation. For example, of the 4112 ground points from the strong beam at night, the 1090 points that passed the spatial filter had a bias, MAD, RMSE and ubRMSE that were 2.4, 2.4, 5.0, and 8.0 times better than the full set of points (0.63, 0.64, 0.77, and 0.44 m vs. 1.51, 1.51, 3.85 and 3.54 m), and approached the metrics for ground points from the sparsely vegetated area (0.53, 0.53, 0.59, and 0.26 m; Fig. 14).

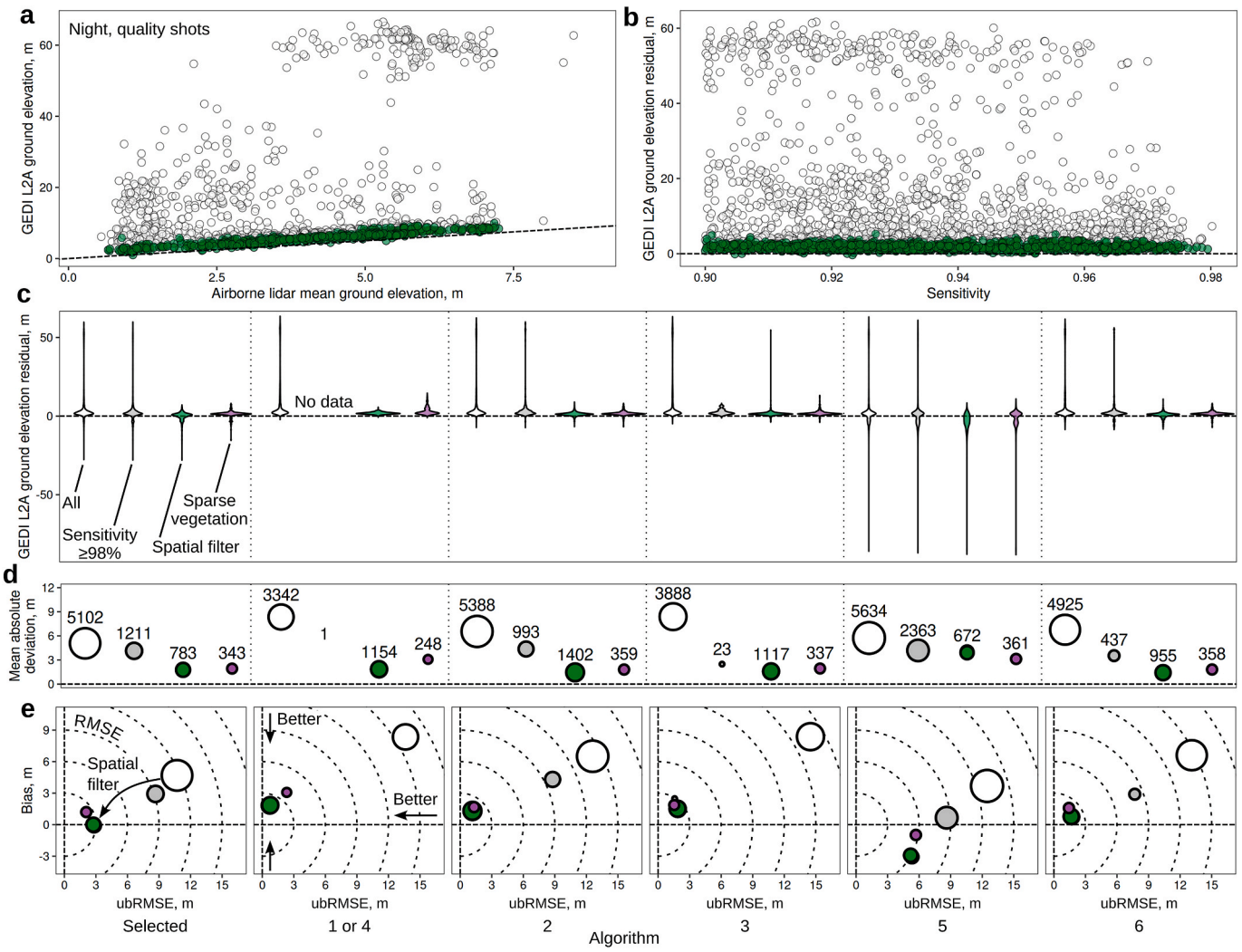

Fig. 9. GEDI ground elevation vs. mean elevation of airborne lidar ground returns in each GEDI shot footprint. (**a**) GEDI L2A ground elevations (algorithm 1, quality-filtered shots at night) vs. mean elevation of airborne lidar ground returns within the 25 m GEDI shot footprint without (white) and with (green) spatial filtering of GEDI ground points. (**b**) Residuals from (a) plotted with respect to GEDI estimated shot sensitivity. (**c**) Distributions of residuals by GEDI waveform-processing algorithm, for all ground elevations (white), shots with sensitivity at least 98% (gray), ground elevations passing the spatial filter (green), and ground elevations within the area of sparse vegetation (purple; see Fig. 4). (**d**) Mean absolute deviations from (c), with number of shots shown above each point and indicated by point area. (**e**) Unbiased RMSE (ubRMSE) and bias as in (d); RMSE is given by distance from the origin. Error metrics from four perturbed spatial filter parameterizations (each parameter increased by 10%) are plotted in (d) and (e) but are indistinguishable. (For interpretation of the references to color in this figure legend, the reader is referred to the Web version of this article.)

3.4. Sensitivity of error metrics to spatial filter parameters

The spatial filters used on GEDI and ATLAS classified up to 8.9% more or 5% fewer points as ground points after each parameter was individually increased by 10% (Fig. 15). Filtering of GEDI and ATLAS point sets was insensitive to a 10% increase in max_distance. Increases in initial_distance and slope make the filters more permissive, and resulted in more points classified as ground. An increase in max_window_size makes the filter more restrictive, and resulted in fewer ATLAS points classified as ground; increasing the large (10 km) maximum window size of the GEDI filter had no effect on the classification of GEDI point sets.

The differences in ground-classified point sets after 10% increases in each filter parameter caused GEDI and ATLAS error metrics to change by −0.174 to 0.041 m (Fig. 15). The error metrics for all the perturbed parameter sets are plotted in Fig. 9d and e, and in Fig. 14c and d, but are visually indistinguishable from the metrics for the unperturbed parameter sets. In most cases, perturbations that made the filter more restrictive (that is, the 10% increase max_window_size for ATLAS) reduced the error, and perturbations that made the filter more permissive (increases in initial_distance and slope) increased the error. The exceptions were GEDI algorithm 5 and the "selected" ground elevations in the L2A product, for which all error metrics were reduced by up to 17.4 cm with more permissive filtering; in addition, increases in the slope parameter reduced error metrics for some other GEDI algorithms by up to 4.5 cm (Fig. 15).

4. Discussion

Both GEDI L2A and ATLAS ATL08 products produced useful terrain data in this tropical peatland, though extracting the useful data was complicated by dense forest canopies (Fig. 2). Dense canopies are known to pose problems for terrain estimation using lidar (Lim et al., 2003; Dubayah et al., 2010; Neuenschwander and Pitts, 2019), and the need to penetrate the dense canopies of tropical forests was part of the

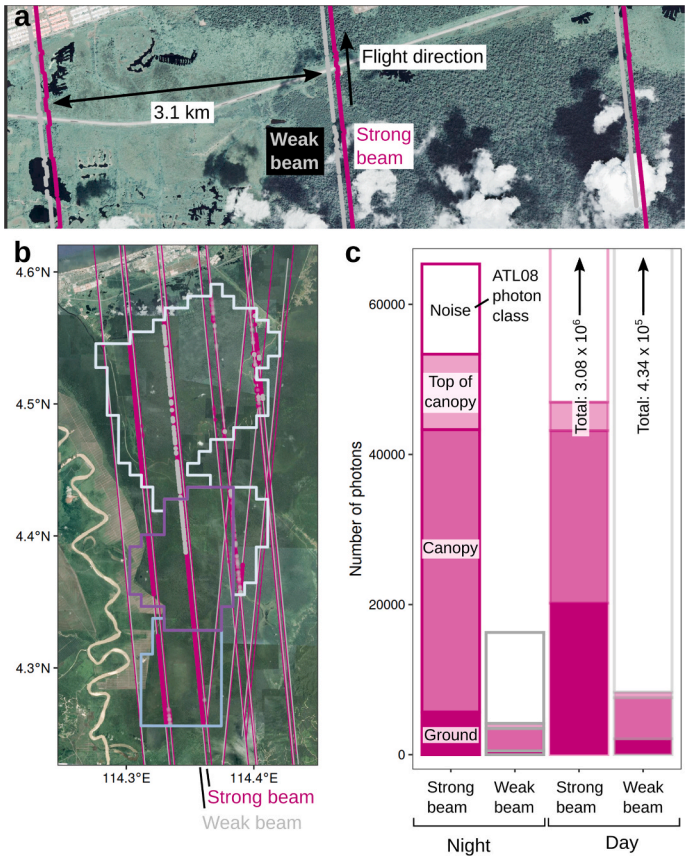

Fig. 10. ATLAS coverage of the study area. (**a**) Beam configuration of ATLAS: reference photons from ATLAS weak and strong beams from a single transit by ICESat-2 of the northwestern edge of the study area. (**b**) ATLAS transects over the study area from the strong (fuchsia) and weak beams (gray). Reference photons for valid data are shown as points (small points: night; smaller points: day). (**c**) Total received photons in the region of airborne lidar coverage from strong and weak beams during the night and day, with filled portions indicating photons classified as ground, canopy, or top-of-canopy photons in the ATL08 product.

motivation for the high energy of GEDI shots (Dubayah et al., 2020). The dense canopy cover in the study area was apparent in the low ground visibility (ratio of ground returns to all returns) in the airborne lidar data: the mean ground visibility in the area of airborne lidar coverage was only 2.83%, with 87.6% of the area having a ground visibility of less than 5% and 47.8% having a ground visibility of less than 2% (Fig. 4). As 98% and 95% canopy cover correspond to the design specifications of the full-power and coverage beams of GEDI, respectively (Dubayah et al., 2020), it is to be expected that GEDI shots did not always detect the ground in this setting. Cases where little, if any, laser energy reached the ground and was reflected back to the instrument can be identified in waveforms without a discernible ground peak (Fig. 7) and ground elevation estimates that lie at or near the top of the canopy (Fig. 8). Similar outliers at the canopy height have been observed in higher-latitude forests with dense canopies using GEDI (Spracklen and Spracklen, 2021), and have also been observed in ATLAS data from tropical peat swamps by Davenport et al. (2020) and Berninger and Siegert (2020).

The difficulty of collecting terrain altimetry in areas with dense vegetation is well known from studies using airborne lidar dating back more than 20 years (Vosselman, 2000; Zhang et al., 2003; Lim et al., 2003). In processing discrete-return airborne lidar data, the established methods for identifying non-ground returns are based on the idea that incoherent jumps in elevation between returns are most likely caused not by ground features, but by non-ground objects. These "objects" may vary in size: in cityscapes, they might be roofs of buildings; in dense forests they might be areas where, by chance, there are no ground returns. In both cases, most ground point classification algorithms remove objects of varying sizes by using a multiscale or hierarchical strategy using spatial information, or "context," from points at a range of scales. If objects in the setting are large, a larger maximum scale of context is required to remove them; in the case of our airborne lidar dataset, a maximum window size of 200 m was needed to effectively remove canopy points from areas without ground returns. These multiscale strategies are highly effective at removing objects while retaining ground features in most settings, and there have not been major improvements in accuracy of ground point classification algorithms in recent years (Chen et al., 2013; Zhang et al., 2016; Zhao et al., 2016).

Our results show that ground point classification algorithms can also be usefully applied to spaceborne lidar ground points, whether from modes in waveforms (GEDI L2A) or from ground-classified photon bounce points (ATLAS ATL08). The basic logic is the same as in ground point classification of airborne lidar datasets: visually, we consider an isolated spike to be more likely attributable to a misclassified canopy return than to a ground feature. A conceptually similar approach is used in the DRAGANN algorithm used to produce the ATL08 data product: nearby photon bounce points are merged into clusters that are interpreted as belonging to ground or canopy surfaces, discarding (classifying as noise) photons that are spatially isolated. Because of power constraints, the number of candidate ground points per area from spaceborne lidar (1.65×10^{-4} quality shots m^{-2} and 0.106 signal photons m^{-2}, from GEDI and ATLAS respectively, in full-power and strong beams at night) is necessarily much lower than in airborne lidar data sets (typically 2–3 m^{-2}; Manuri et al., 2017). Given the lower spatial density of candidate ground points in spaceborne lidar data, for ground points to be distinguishable from canopy points, the ground surface must be smoother. Thus, part of the reason that a spatial filtering approach works in this setting is that, because of the mechanism of peat accumulation (Cobb et al., 2017), the ground surface is smooth at the landscape scale (Manuri et al., 2017).

In more complex terrain, spatial filters could be difficult to apply, especially on GEDI data, for which the smallest scale of spatial information is the 60 m along-track shot spacing. The difficulties created by complex terrain are easy to picture when examining profiles (Fig. 8): in a setting where some of the "spikes" in GEDI ground elevation estimates might plausibly represent a terrain feature, parameters that remove canopy returns could also artificially smooth out the terrain. In particular, the problems created by tall vegetation on steep slopes, much explored in studies of GLAS data (Lefsky et al., 2007; Hilbert and Schmullius, 2012) and also relevant to GEDI (Adam et al., 2020; Spracklen and Spracklen, 2021), will not be solved by this approach, and will require other strategies such as filtering by estimated canopy cover (Tang and Armston, 2019) or considering constraints on reasonable foliage profiles (Tang et al., 2014).

The limitation of spatial filtering strategies to smooth terrain may be relaxed somewhat as the spatial density of GEDI and ATLAS data continues to increase until the end of these missions. Note, however, that our current implementation works on one spaceborne lidar track at a time, using only the along-track position of ground elevation estimates; filtering data from multiple tracks together could be possible with some algorithms, but strongly uneven point density (caused by gaps between tracks) creates additional challenges (Roberts et al., 2019). Spatial filtering of spaceborne lidar data will also require adaptation in studies of peatland terrain that include steep edges, such as scars from fires that have burnt away part of the peat surface (Ballhorn et al., 2009; Simpson et al., 2016).

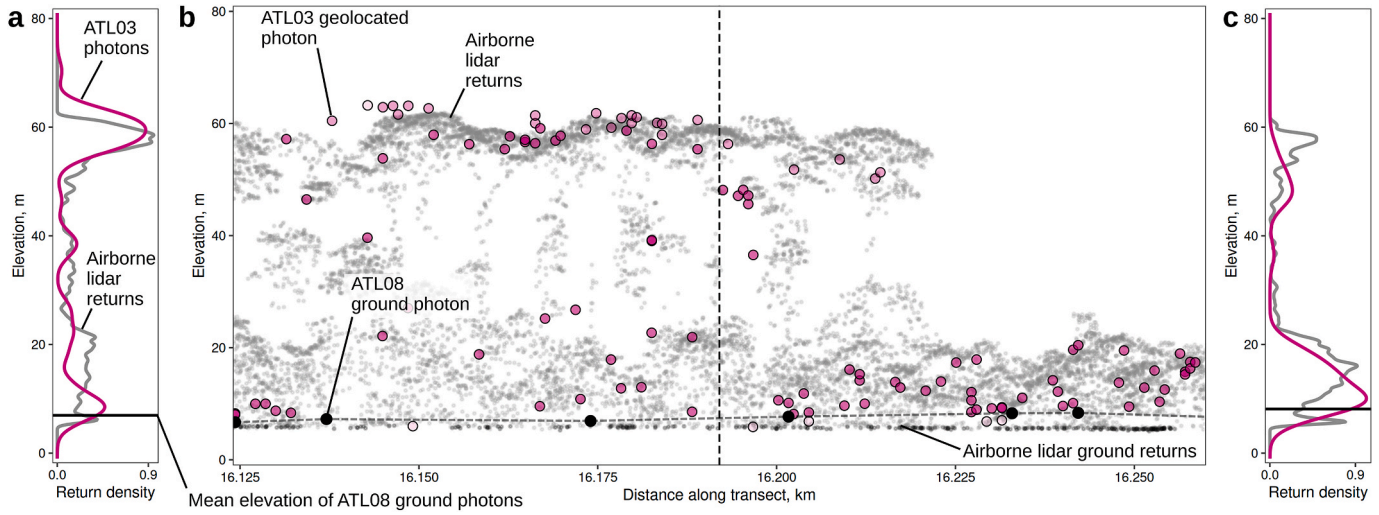

Fig. 11. Profiles of ATLAS photons (fuchsia) from strong beams at night, and airborne lidar returns (gray). (**a, c**) Sample ATLAS photon pseudowaveforms and airborne lidar return pseudowaveforms, constructed using a kernel density estimator with different bandwidths for airborne lidar returns (gray) and ATLAS photons (fuchsia). (**b**) ATLAS photons and airborne lidar returns used to construct the pseudowaveforms (a, c).

After the removal of canopy outliers with spatial filters, ground elevations from both GEDI L2A and ATL08 remained higher than corresponding airborne lidar ground elevations by 183.1 cm (average from algorithm 1 quality shots) and 63.4 cm (average from strong beams at night) respectively. GEDI L2A (algorithms 1–4 and 6) and ATL08 ground elevations were also higher than corresponding airborne lidar ground points in the sparsely vegetated part of the study area (Figs. 9 and 14). (Filtered GEDI ground elevations from waveform processing algorithm 5 and from "selected" ground points had offsets that were negative because of negative outliers, which resulted in a relatively low precision,

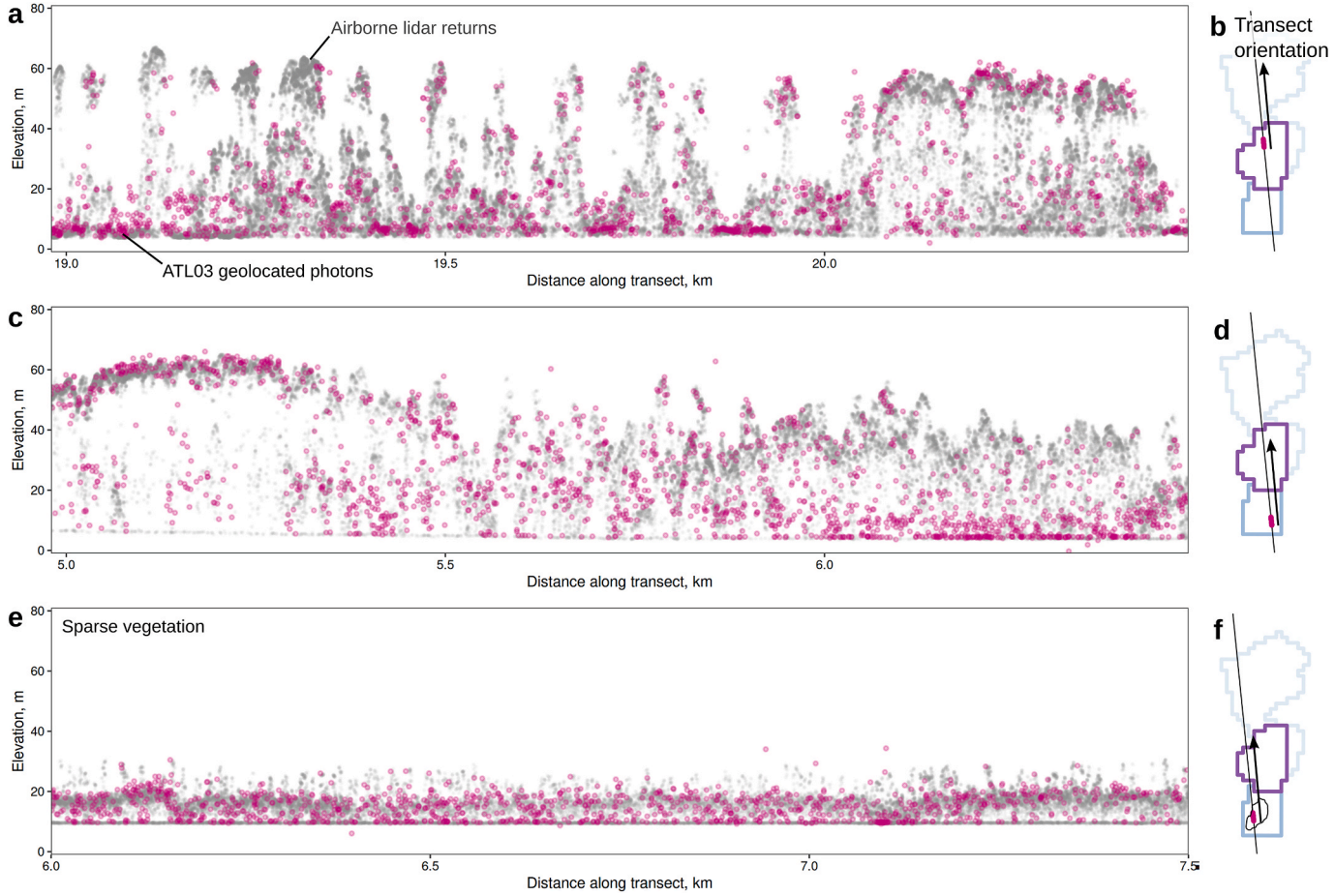

Fig. 12. Profiles of ATLAS photons (fuchsia) from strong beams at night, and airborne lidar returns (gray). (**a, c, e**) Airborne lidar returns within 8.5 m of the ATLAS transect center line (gray) and ATL08 signal photons. (**b, c, f**) Locations of profiles (a, c, e) in study area.

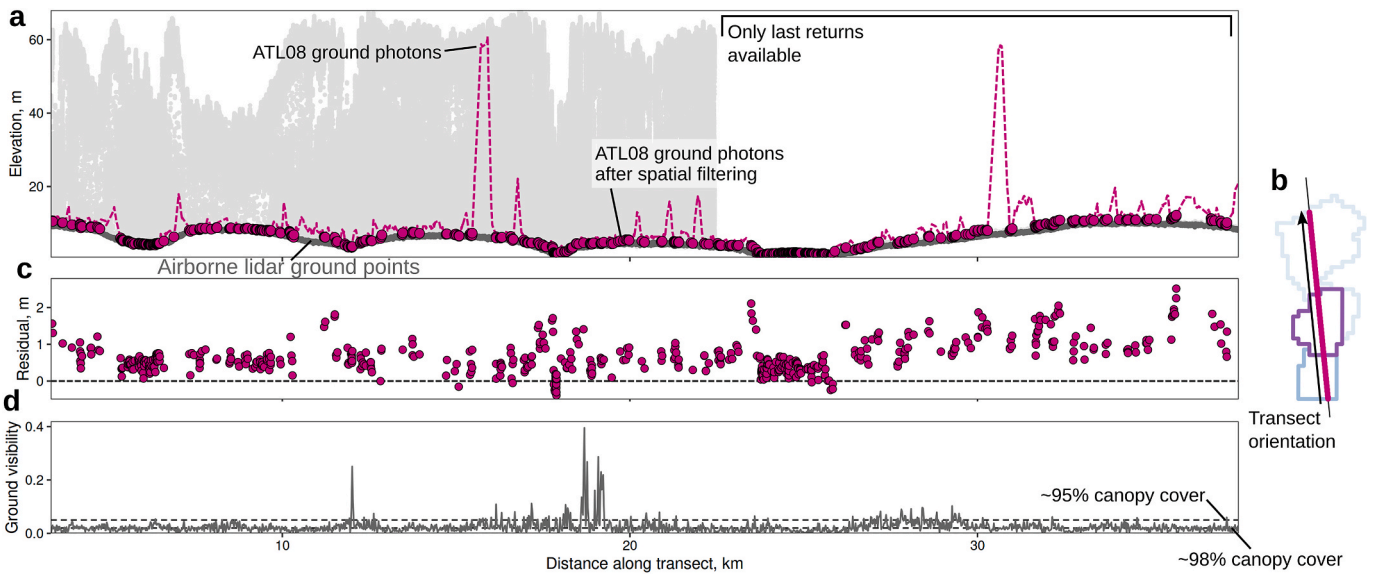

Fig. 13. ATLAS ground elevations. (**a**) ATL08 ground photon bounce points from a strong beam at night before (fuchsia dashed line) and after spatial filtering (points), and airborne lidar ground returns (gray). (**b**) Ground visibility estimated from airborne lidar data along the transect. (**c**) Location of transect shown in (a, b).

indicated by a high ubRMSE.) We briefly consider four possible explanations for the higher ground elevation estimates from GEDI and ATLAS data: (1) surface changes (peat accumulation) between the time of acquisition of the airborne lidar and the GEDI and ATLAS data; (2) geolocation and altimetric errors in the spaceborne lidar datasets; (3) difference in vertical datum; and (4) peat surface microtopography.

Although the airborne lidar data were collected 10–11 years before the ATLAS and GEDI data, the higher elevations in the spaceborne lidar datasets cannot be explained by peat accumulation (explanation 1): a typical rate of peat accumulation in coastal Southeast Asia peatlands, including at this site (Dommain et al., 2015), is 2 mm/y (Dommain et al., 2011). This accumulation rate yields an increase in surface elevation of about 2 cm, too small to explain the higher ground elevations obtained from GEDI and ATLAS.

As for geolocation and altimetric errors for the two missions (explanation 2), because of the small terrain gradients at the site, geolocation errors have little effect on ground elevations: with a 1 m/km surface gradient, a 10–20 m geolocation error, as estimated for GEDI's early calibrated data products (Dubayah et al., 2020), introduces just a 1–2 cm bias, and therefore geolocation errors could not contribute significant average vertical offsets in this setting. Altimetric errors in ATL03 photon bounce points were found to be better than 5 cm in an evaluation on the Antarctic Ice Sheet (Brunt et al., 2019), and a comparison of airborne lidar and ATLAS terrain elevations across non-tundra sites from the United States National Ecological Observatory Network (NEON) found a −20 cm offset between ATLAS and airborne lidar terrain elevations (Liu et al., 2021). The same comparison found a 117 cm difference in offset between ATLAS and GEDI terrain elevations, similar to the 119.7 cm difference found here, so it is possible that the same source of error could explain the difference in offsets that we observed between GEDI and ATLAS elevations. As the vertical datum for the airborne lidar data is unknown (explanation 3), difference between this datum and the EGM96 geoid to which we transformed the GEDI and ATLAS elevations could explain a constant offset between the airborne and spaceborne lidar elevations, though not the difference in offset between GEDI and ATLAS ground elevations.

Finally, elevation offsets between airborne lidar, GEDI and ATLAS data could be affected by the hummock-hollow microtopography of about 30–50 cm relief found in our study area as well as other peatlands in this region (explanation 4; Lampela et al., 2016; Cobb et al., 2017). Because of this microtopographic relief, the airborne lidar, GEDI and ATLAS datasets are likely to differ in the subset of reflecting surfaces sensed and classified as ground. In the case of GEDI, the ground elevation is obtained from a peak (mode) in the waveform, which could lie somewhere between the elevations of local depressions (hollows) and local high points (hummocks) in the peat surface, whereas spatial filtering of airborne lidar data could remove many of the returns from hummocks (Fig. 6). Similarly, because of their sparseness, ATLAS photon bounce points from hummocks might be accepted by a spatial filter more often than returns from hummocks in airborne lidar datasets (Fig. 11), which could result in a higher average elevation in spatially filtered ATL08 ground elevations than in spatially filtered airborne lidar returns.

Notwithstanding these residual elevation offsets relative to the airborne lidar dataset, both GEDI (algorithm 1 or 4) and nighttime ATLAS ground points captured the overall terrain shape well after spatial filtering, with relatively low ubRMSE (71.5 cm and 44.5 cm, for quality shots and for strong beams at night, respectively, reduced from 1362.0 cm to 353.7 cm before filtering). Even with the vertical offsets included, RMSE values from the spatially filtered GEDI and ATLAS data (196.6 cm with GEDI algorithm 1 quality shots, 77.4 cm with ATLAS strong beams at night) compare favorably to the RMSEs of 403 cm and 224 cm observed for terrain elevations from GEDI and ATLAS, respectively, across non-tundra NEON sites (Liu et al., 2021).

We found that error metrics of filtered GEDI and ATLAS data were relatively insensitive to perturbation of the parameters of the spatial filter we used (PMF; Zhang et al., 2003). Increases of 10% in each parameter yielded small changes in error metrics (−0.174 to 0.041 m). Further, starting with a basic knowledge of site terrain and vegetation, we arrived at the parameters after minimal trial and error, without optimization or reference to airborne lidar data. Though other spatial filters use different parameters, these findings suggest that there is a large region of parameter space in which the error metrics of filtered ground points from these peatlands are excellent.

The availability of terrain elevations in densely forested tropical peatlands via spatial filtering of GEDI and ATLAS data has several benefits. First, the ability to derive useful ground points from these products provides terrain data from peatlands all over the tropics for free, including in places that are remote and inaccessible (Lähteenoja and Page, 2011; Dargie et al., 2017; Hastie et al., 2022). Second, more accurate ground elevations in these settings also enable more accurate canopy height estimates, because canopy heights are obtained by subtracting top-of-canopy elevations from the ground elevation (Hofton and Blair, 2019), and thus can only be as accurate as the ground elevations. Third, the success of this approach in tropical peatlands suggests a

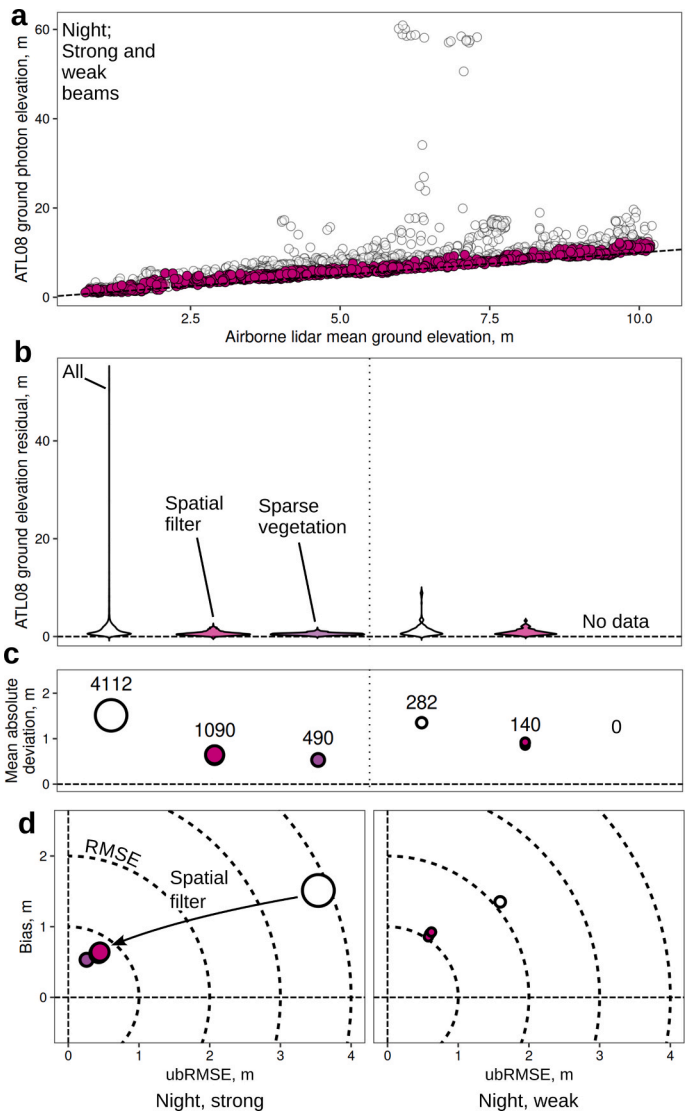

Fig. 14. ATLAS ground elevations vs. airborne lidar ground returns in the ATLAS shot footprint. (**a**) Elevations of ATL08 ground photon bounce points passing quality criteria (night) vs. mean elevation of airborne lidar ground returns within the 11 m ATLAS shot footprint without (white) and with (fuchsia) spatial filtering of ATL08 ground points. (**b**) Distributions of residuals from strong and weak beams at night without (white) and with (fuchsia) spatial filtering of ATLAS ground points, and from the area of sparse vegetation (purple; see Fig. 4). (**c**) Mean absolute deviations from (b), with number of photons shown above each point and indicated by point area. (**d**) Unbiased RMSE and bias as in (c); RMSE is given by distance from the origin. Error metrics from four perturbed spatial filter parameterizations (each parameter increased by 10%) are plotted in (c) and (d) but are indistinguishable. (For interpretation of the references to color in this figure legend, the reader is referred to the Web version of this article.)

strategy to explore in other environments: spatial filters could be useful tools for finding misclassified ground points wherever the terrain is known to be smooth.

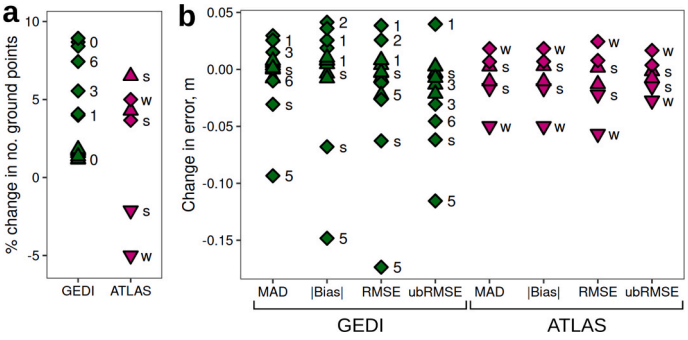

Fig. 15. Sensitivity of spaceborne lidar ground point classification to spatial filter parameters. (**a**) Percent change in the number of GEDI (green) and ATLAS (fuchsia) points classified as ground after a 10% increase in each filter parameter, one at a time: initial_distance (up triangles); slope (diamonds); max_window_size (down triangles). Filtering of ATLAS points was insensitive to a 10% increase in max_window_size (not shown); filtering of all point sets was insensitive to a 10% increase in max_distance. Annotations on GEDI points indicate ground points obtained from the lowest mode identified by each GEDI waveform processing algorithm (1–6) or the selected ("s") mode in the GEDI L2A product; annotations on ATLAS points indicate strong ("s") vs. weak ("w") beam at night. (**b**) Change in error metrics after a 10% increase in each filter parameter: mean absolute difference (MAD); absolute bias (|Bias|); root-mean-squared error (RMSE); unbiased root-mean-squared error (ubRMSE). (For interpretation of the references to color in this figure legend, the reader is referred to the Web version of this article.)

5. Conclusions

Tropical peatlands are landscapes that consist entirely of organic matter and are now threatened by drainage that enables catastrophic fire and globally significant greenhouse gas emissions. Mitigation of peatland drainage requires terrain data that are difficult to obtain from densely forested peatlands. Fortunately, the challenge of estimating tropical peatland terrain is well matched by the strengths and limitations of GEDI and ATLAS spaceborne lidar products. The density of peat forest canopies can cause reflections from the mid- or upper canopy to be misinterpreted as ground points. However, we found that these outliers could be removed using spatial filters typically applied to airborne lidar. Spatial filtering of GEDI L2A algorithm 1 quality data reduced MAD, RMSE and ubRMSE from 8.35, 15.98 and 13.62 m to 1.83, 1.97, and 0.72 m. Similarly, spatial filtering of ATLAS ATL08 ground photons from strong beams at night reduced MAD, RMSE, and ubRMSE from 1.51, 3.85 and 3.54 m to 0.64, 0.77 and 0.44 m. These improvements were facilitated by the low relief of the underlying terrain. In complex terrain, this approach could be difficult to apply, especially on GEDI data, for which the smallest scale of spatial information is the 60 m along-track spacing. Nonetheless, spatial filters could be useful tools for finding misclassified ground points in settings, like peatlands (Cobb et al., 2017), in which the surface is known to be smooth on a landscape scale.

Funding

This research was supported by the National Research Foundation Singapore through the Singapore-MIT Alliance for Research and Technology's Center for Environmental Sensing and Modeling interdisciplinary research program and through Grant No. NRF2019-ITC001-001, by the US National Science Foundation under grant number 1923491, and by the Office for Space Technology and Industry (OSTIn), Singapore's national space office, through its Space Technology Development Programme (Grant No. S22-02005-STDP).

Declaration of competing interest

The authors declare that they have no known competing financial interests or personal relationships that could have appeared to influence the work reported in this paper.

Data availability

Data will be made available on request.

Acknowledgments

GEDI L1B and L2A data were provided by the NASA EOSDIS LP DAAC (Land Processes Distributed Active Archive Center), ATLAS ATL03 and ATL08 data by the NASA National Snow and Ice Data Center Distributed Active Archive Center, and airborne lidar data by the Survey Department of Brunei Darussalam.

References

Abdalati, W., Zwally, H.J., Bindschadler, R., Csatho, B., Farrell, S.L., Fricker, H.A., Harding, D., Kwok, R., Lefsky, M., Markus, T., Marshak, A., Neumann, T., Palm, S., Schutz, B., Smith, B., Spinhirne, J., Webb, C., 2010. The ICESat-2 laser altimetry mission. Proc. IEEE 98, 735–751. https://doi.org/10.1109/jproc.2009.2034765.

Adam, M., Urbazaev, M., Dubois, C., Schmullius, C., 2020. Accuracy assessment of GEDI terrain elevation and canopy height estimates in European temperate forests: influence of environmental and acquisition parameters. Rem. Sens. 12, 3948. https://doi.org/10.3390/rs12233948.

Anderson, J.A.R., 1961. The Ecology and Forest Types of the Peat Swamp Forests of Sarawak and Brunei in Relation to Their Silviculture. Ph.D. thesis. The University of Edinburgh.

Anderson, J.A.R., 1963. The flora of the peat swamp forests of Sarawak and Brunei, including a catalogue of all recorded species of flowering plants, ferns and fern allies. Gard. Bull. Singap. 20, 131–228.

Anderson, J.A.R., 1964. The structure and development of the peat swamps of Sarawak and Brunei. J. Trop. Geogr. 18, 7–16.

Anderson, J.A.R., 1983. The tropical peat swamps of western Malesia. In: Gore, A.J.P. (Ed.), Mires: Swamp, Bog, Fen and Moor: Regional Studies, Ecosystems of the World, 4B. Elsevier, Amsterdam, The Netherlands, pp. 181–199.

Armston, J., Disney, M., Lewis, P., Scarth, P., Phinn, S., Lucas, R., Bunting, P., Goodwin, N., 2013. Direct retrieval of canopy gap probability using airborne waveform lidar. Remote Sens. Environ. 134, 24–38. https://doi.org/10.1016/j.rse.2013.02.021.

Axelsson, P., 2000. DEM generation from laser scanner data using adaptive TIN models. Int. J. Appl. Earth Obs. Geoinf. 33, 110–117.

Ballhorn, U., Jubanski, J., Siegert, F., 2011. ICESat/GLAS data as a measurement tool for peatland topography and peat swamp forest biomass in Kalimantan, Indonesia. Rem. Sens. 3, 1957–1982. https://doi.org/10.3390/rs3091957.

Ballhorn, U., Siegert, F., Mason, M., Limin, S., 2009. Derivation of burn scar depths and estimation of carbon emissions with LIDAR in Indonesian peatlands. P. Natl. Acad. Sci. 106, 21213–21218. https://doi.org/10.1073/pnas.0906457106.

Berninger, A., Siegert, F., 2020. The potential of ICESat-2 to identify carbon-rich peatlands in Indonesia. Rem. Sens. 12, 4175. https://doi.org/10.3390/rs12244175.

Blair, J.B., Hofton, M.A., 1999. Modeling laser altimeter return waveforms over complex vegetation using high-resolution elevation data. Geophys. Res. Lett. 26, 2509–2512. https://doi.org/10.1029/1999gl010484.

Bleeker, P., 1983. Soils of Papua New Guinea. Australian National University, Canberra, Australia.

Brunt, K.M., Neumann, T.A., Smith, B.E., 2019. Assessment of ICESat-2 ice sheet surface heights, based on comparisons over the interior of the Antarctic ice sheet. Geophys. Res. Lett. 46, 13072–13078. https://doi.org/10.1029/2019gl084886.

Chen, C., Li, Y., Li, W., Dai, H., 2013. A multiresolution hierarchical classification algorithm for filtering airborne LiDAR data. ISPRS J. Photogrammetry Remote Sens. 82, 1–9. https://doi.org/10.1016/j.isprsjprs.2013.05.001.

Cobb, A.R., Dommain, R., Tan, F., Heng, N.H.E., Harvey, C.F., 2020. Carbon storage capacity of tropical peatlands in natural and artificial drainage networks. Environ. Res. Lett. 15, 114009 https://doi.org/10.1088/1748-9326/aba867.

Cobb, A.R., Hoyt, A.M., Gandois, L., Eri, J., Dommain, R., Abu Salim, K., Kai, F.M., Haji Su'ut, N.S., Harvey, C.F., 2017. How temporal patterns in rainfall determine the geomorphology and carbon fluxes of tropical peatlands. P. Natl. Acad. Sci. 114, E5187–E5196. https://doi.org/10.1073/pnas.1701090114.

Dargie, G.C., Lewis, S.L., Lawson, I.T., Mitchard, E.T.A., Page, S.E., Bocko, Y.E., Ifo, S.A., 2017. Age, extent and carbon storage of the central Congo Basin peatland complex. Nature 542, 86–90. https://doi.org/10.1038/nature21048.

Davenport, I.J., McNicol, I., Mitchard, E.T.A., Dargie, G., Suspense, I., Milongo, B., Bocko, Y.E., Hawthorne, D., Lawson, I., Baird, A.J., Page, S., Lewis, S.L., 2020. First evidence of peat domes in the Congo Basin using LiDAR from a fixed-wing drone. Rem. Sens. 12, 2196. https://doi.org/10.3390/rs12142196.

Dohong, A., Aziz, A.A., Dargusch, P., 2018. A review of techniques for effective tropical peatland restoration. Wetlands 38, 275–292. https://doi.org/10.1007/s13157-018-1017-6.

Dommain, R., Cobb, A.R., Joosten, H., Glaser, P.H., Chua, A.F.L., Gandois, L., Kai, F.M., Noren, A., Abu Salim, K., Haji Su'ut, N.S., Harvey, C.F., 2015. Forest dynamics and tip-up pools drive pulses of high carbon accumulation rates in a tropical peat dome in Borneo (Southeast Asia). J. Geophys. Res-Biogeo. 120, 617–640. https://doi.org/10.1002/2014JG002796.

Dommain, R., Couwenberg, J., Joosten, H., 2011. Development and carbon sequestration of tropical peat domes in south-east Asia: links to post-glacial sea-level changes and Holocene climate variability. Quat. Sci. Rev. 30, 999–1010. https://doi.org/10.1016/j.quascirev.2011.01.018.

Draper, F.C., Roucoux, K.H., Lawson, I.T., Mitchard, E.T.A., Honorio Coronado, E.N., Lähteenoja, O., Montenegro, L.T., Sandoval, E.V., Zaráte, R., Baker, T.R., 2014. The distribution and amount of carbon in the largest peatland complex in Amazonia. Environ. Res. Lett. 9, 124017 https://doi.org/10.1088/1748-9326/9/12/124017.

Dubayah, R., Blair, J.B., Goetz, S., Fatoyinbo, L., Hansen, M., Healey, S., Hofton, M., Hurtt, G., Kellner, J., Luthcke, S., Armston, J., Tang, H., Duncanson, L., Hancock, S., Jantz, P., Marselis, S., Patterson, P.L., Qi, W., Silva, C., 2020. The global ecosystem dynamics investigation: high-resolution laser ranging of the earth's forests and topography. Sci. Remote Sens. 1, 100002 https://doi.org/10.1016/j.srs.2020.100002.

Dubayah, R., Hofton, M., Blair, J., Armston, J., Tang, H., Luthcke, S., 2022a. GEDI L2A elevation and height metrics data global footprint level v002. URL: https://lpdaac.usgs.gov/products/gedi02_av002/. (Accessed 29 June 2022).

Dubayah, R., Luthcke, S., Blair, J., Hofton, M., Armston, J., Tang, H., 2022b. GEDI L1B geolocated waveform data global footprint level V002. URL: https://lpdaac.usgs.gov/products/gedi01_bv002/. (Accessed 29 June 2022).

Dubayah, R.O., Sheldon, S.L., Clark, D.B., Hofton, M.A., Blair, J.B., Hurtt, G.C., Chazdon, R.L., 2010. Estimation of tropical forest height and biomass dynamics using lidar remote sensing at La Selva, Costa Rica. J. Geophys. Res-Biogeo. 115, G00E09. https://doi.org/10.1029/2009jg000933.

Evans, J.S., Hudak, A.T., 2007. A multiscale curvature algorithm for classifying discrete return LiDAR in forested environments. IEEE Trans. Geosci. Rem. Sens. 45, 1029–1038. https://doi.org/10.1109/tgrs.2006.890412.

Évrard, C., 1968. Recherches écologiques sur le peuplement forestier des sols hydromorphes de la Cuvette centrale congloaise. Institut National pour l'Étude Agronomique du Congo, Bruxelles. Série scientifique, no. 110.

Frappart, F., Blarel, F., Fayad, I., Bergé-Nguyen, M., Crétaux, J.F., Shu, S., Schregenberger, J., Baghdadi, N., 2021. Evaluation of the performances of radar and lidar altimetry missions for water level retrievals in mountainous environment: the case of the Swiss lakes. Rem. Sens. 13, 2196. https://doi.org/10.3390/rs13112196.

Harding, D., Lefsky, M., Parker, G., Blair, J., 2001. Laser altimeter canopy height profiles: methods and validation for closed-canopy, broadleaf forests. Remote Sens. Environ. 76, 283–297. https://doi.org/10.1016/s0034-4257(00)00210-8.

Harding, D.J., Carabajal, C.C., 2005. ICESat waveform measurements of within-footprint topographic relief and vegetation vertical structure. Geophys. Res. Lett. 32 https://doi.org/10.1029/2005gl023471.

Hastie, A., Coronado, E.N.H., Reyna, J., Mitchard, E.T.A., Åkesson, C.M., Baker, T.R., Cole, L.E.S., Oroche, C.J.C., Dargie, G., Dávila, N., Grandi, E.C.D., Águila, J.D., Torres, D.D.C., Paiva, R.D.L.C., Draper, F.C., Flores, G., Grández, J., Hergoualc'h, K., Householder, J.E., Janovec, J.P., Lähteenoja, O., Reyna, D., Rodríguez-Veiga, P., Roucoux, K.H., Tobler, M., Wheeler, C.E., Williams, M., Lawson, I.T., 2022. Risks to carbon storage from land-use change revealed by peat thickness maps of Peru. Nat. Geosci. 15, 369–374. https://doi.org/10.1038/s41561-022-00923-4.

Hilbert, C., Schmullius, C., 2012. Influence of surface topography on ICESat/GLAS forest height estimation and waveform shape. Rem. Sens. 4, 2210–2235. https://doi.org/10.3390/rs4082210.

Hofton, M., Blair, J.B., 2019. Algorithm Theoretical Basis Document (ATBD) for GEDI Transmit and Receive Waveform Processing for L1 and L2 Products. Technical Report. National Aeronautics and Space Administration. Goddard Space Flight Center, Greenbelt, Maryland, USA. Version 1.0.

Honorio Coronado, E.N., Hastie, A., Reyna, J., Flores, G., Grández, J., Lähteenoja, O., Draper, F.C., Åkesson, C.M., Baker, T.R., Bhomia, R.K., Cole, L.E.S., Dávila, N., Águila, J.D., Águila, M.D., Torres, D.D.C., Lawson, I.T., Brañas, M.M., Mitchard, E.T.A., Monteagudo, A., Phillips, O.L., Ramírez, E., Ríos, M., Ríos, S., Rodriguez, L., Roucoux, K.H., Casapia, X.T., Vasquez, R., Wheeler, C.E., Montoya, M., 2021. Intensive field sampling increases the known extent of carbon-rich Amazonian peatland pole forests. Environ. Res. Lett. 16, 074048 https://doi.org/10.1088/1748-9326/ac0e65.

Hooijer, A., 2005. Hydrology of tropical wetland forests: recent research results from Sarawak peatswamps. In: Bonell, M., Bruijnzeel, L.A. (Eds.), Forests, Water and People in the Humid Tropics, vol. 17. Cambridge University Press, Cambridge, UK, pp. 447–461.

Hooijer, A., Page, S., Jauhiainen, J., Lee, W.A., Lu, X.X., Idris, A., Anshari, G., 2012. Subsidence and carbon loss in drained tropical peatlands. Biogeosciences 9, 1053–1071. https://doi.org/10.5194/bg-9-1053-2012.

Jaenicke, J., Rieley, J.O., Mott, C., Kimman, P., Siegert, F., 2008. Determination of the amount of carbon stored in Indonesian peatlands. Geoderma 147, 151–158. https://doi.org/10.1016/j.geoderma.2008.08.008.

Kraus, K., Pfeifer, N., 2001. Advanced DTM generation from LiDAR data. Int. J. Appl. Earth Obs. Geoinf. 34, 23–30.

Lähteenoja, O., Page, S., 2011. High diversity of tropical peatland ecosystem types in the Pastaza-Marañón basin, Peruvian Amazonia. J. Geophys. Res. 116, G02025 https://doi.org/10.1029/2010jg001508.

Lähteenoja, O., Ruokolainen, K., Schulman, L., Alvarez, J., 2009. Amazonian floodplains harbour minerotrophic and ombrotrophic peatlands. Catena 79, 140–145. https://doi.org/10.1016/j.catena.2009.06.006.
Lampela, M., Jauhiainen, J., Kämäri, I., Koskinen, M., Tanhuanpää, T., Valkeapää, A., Vasander, H., 2016. Ground surface microtopography and vegetation patterns in a tropical peat swamp forest. Catena 139, 127–136. https://doi.org/10.1016/j.catena.2015.12.016.
Lefsky, M.A., Keller, M., Pang, Y., de Camargo, P.B., Hunter, M.O., 2007. Revised method for forest canopy height estimation from Geoscience Laser Altimeter System waveforms. J. Appl. Remote Sens. 1, 013537 https://doi.org/10.1117/1.2795724.
Leifeld, J., Wüst-Galley, C., Page, S., 2019. Intact and managed peatland soils as a source and sink of GHGs from 1850 to 2100. Nat. Clim. Change 9, 945–947. https://doi.org/10.1038/s41558-019-0615-5.
Lim, K., Treitz, P., Wulder, M., St-Onge, B., Flood, M., 2003. LiDAR remote sensing of forest structure. Prog. Phys. Geogr. 27, 88–106. https://doi.org/10.1191/0309133303pp360ra.
Liu, A., Cheng, X., Chen, Z., 2021. Performance evaluation of GEDI and ICESat-2 laser altimeter data for terrain and canopy height retrievals. Remote Sens. Environ. 264, 112571 https://doi.org/10.1016/j.rse.2021.112571.
Liu, X., 2008. Airborne LiDAR for DEM generation: some critical issues. Prog. Phys. Geogr. 32, 31–49. https://doi.org/10.1177/0309133308089496.
Lovell, J.L., Jupp, D.L.B., Culvenor, D.S., Coops, N.C., 2003. Using airborne and ground-based ranging lidar to measure canopy structure in Australian forests. Can. J. Rem. Sens. 29, 607–622. https://doi.org/10.5589/m03-026.
Luthcke, S.B., Thomas, T.C., Pennington, T.A., Rebold, T.W., Nicholas, J.B., Rowlands, D. D., Gardner, A.S., Bae, S., 2021. ICESat-2 pointing calibration and geolocation performance. Earth Space Sci. 8 https://doi.org/10.1029/2020ea001494.
Magruder, L., Brunt, K., Neumann, T., Klotz, B., Alonzo, M., 2021. Passive ground-based optical techniques for monitoring the on-orbit ICESat-2 altimeter geolocation and footprint diameter. Earth Space Sci. 8 https://doi.org/10.1029/2020ea001414.
Mallet, C., Bretar, F., 2009. Full-waveform topographic lidar: state-of-the-art. ISPRS J. Photogrammetry Remote Sens. 64, 1–16. https://doi.org/10.1016/j.isprsjprs.2008.09.007.
Manuri, S., Andersen, H.E., McGaughey, R.J., Brack, C., 2017. Assessing the influence of return density on estimation of lidar-based aboveground biomass in tropical peat swamp forests of Kalimantan, Indonesia. Int. J. Appl. Earth Obs. Geoinf. 56, 24–35. https://doi.org/10.1016/j.jag.2016.11.002.
Miettinen, J., Hooijer, A., Vernimmen, R., Liew, S.C., Page, S.E., 2017. From carbon sink to carbon source: extensive peat oxidation in insular Southeast Asia since 1990. Environ. Res. Lett. 12, 024014 https://doi.org/10.1088/1748-9326/aa5b6f.
Neuenschwander, A., Pitts, K., 2019. The ATL08 land and vegetation product for the ICESat-2 mission. Remote Sens. Environ. 221, 247–259. https://doi.org/10.1016/j.rse.2018.11.005.
Neuenschwander, A., Guenther, E., White, J.C., Duncanson, L., Montesano, P., 2020. Validation of ICESat-2 terrain and canopy heights in boreal forests. Remote Sens. Environ. 251, 112110 https://doi.org/10.1016/j.rse.2020.112110.
Neuenschwander, A.L., Pitts, K.L., Jelley, B.P., Robbins, J., Klotz, B., Popescu, S.C., Nelson, R.F., Harding, D., Pederson, D., Sheridan, R., 2022a. ATLAS/ICESat-2 L3A Land and Vegetation Height. version 5. http://nsidc.org/data/atl08/versions/5. (Accessed 29 June 2022).
Neuenschwander, A.L., Popescu, S.C., Nelson, R.F., Harding, D.J., Pitts, K.L., Robbins, J. W., 2022b. ATLAS/ICESat-2 L3A Land and Vegetation Height. Version 5 User Guide. NASA National Snow and Ice Data Center, Boulder, Colorado, USA. Updated 26 May 2022.
Neumann, T.A., Brenner, A., Hancockp, D., Robbins, J., Saba, J., Harbeck, K., Gibbons, A., Lee, J., Luthcke, S.B., et al., T.R, 2022. AATLAS/ICESat-2 L2A global geolocated photon data version 5. http://nsidc.org/data/atl03/versions/5. (Accessed 29 June 2022).
Neumann, T.A., Martino, A.J., Markus, T., Bae, S., Bock, M.R., Brenner, A.C., Brunt, K.M., Cavanaugh, J., Fernandes, S.T., Hancock, D.W., Harbeck, K., Lee, J., Kurtz, N.T., Luers, P.J., Luthcke, S.B., Magruder, L., Pennington, T.A., Ramos-Izquierdo, L., Rebold, T., Skoog, J., Thomas, T.C., 2019. The Ice, Cloud, and Land Elevation Satellite–2 mission: A global geolocated photon product derived from the Advanced Topographic Laser Altimeter System. Remote Sens. Environ. 233, 111325 https://doi.org/10.1016/j.rse.2019.111325.
Ni-Meister, W., Jupp, D., Dubayah, R., 2001. Modeling lidar waveforms in heterogeneous and discrete canopies. IEEE Trans. Geosci. Rem. Sens. 39, 1943–1958. https://doi.org/10.1109/36.951085.
Ollinger, S.V., 2010. Sources of variability in canopy reflectance and the convergent properties of plants. New Phytol. 189, 375–394. https://doi.org/10.1111/j.1469-8137.2010.03536.x.
Page, S.E., Hooijer, A., 2016. In the line of fire: the peatlands of Southeast Asia. Philos. T. R. Soc. B. 371, 20150176 https://doi.org/10.1098/rstb.2015.0176.
Page, S.E., Rieley, J.O., Banks, C.J., 2011. Global and regional importance of the tropical peatland carbon pool. Glob. Change Biol. 17, 798–818. https://doi.org/10.1111/j.1365-2486.2010.02279.x.
Pingel, T.J., Clarke, K.C., McBride, W.A., 2013. An improved simple morphological filter for the terrain classification of airborne LIDAR data. ISPRS J. Photogrammetry Remote Sens. 77, 21–30. https://doi.org/10.1016/j.isprsjprs.2012.12.002.
Polak, B., 1933. Ueber Torf and Moor in Niederländisch indien. Verhandelingen der Koninklijke Akademie van Wetenschappen te Amsterdam Afdeeling Natuurkunde (Tweede Sectie) 30, 1–85.
Popescu, S.C., Zhao, K., Neuenschwander, A., Lin, C., 2011. Satellite lidar vs. small footprint airborne lidar: comparing the accuracy of aboveground biomass estimates and forest structure metrics at footprint level. Remote Sens. Environ. 115, 2786–2797. https://doi.org/10.1016/j.rse.2011.01.026.
Richards, P., 1952. The Tropical Rain Forest. Cambridge University Press, Cambridge, UK.
Roberts, K.C., Lindsay, J.B., Berg, A.A., 2019. An analysis of ground-point classifiers for terrestrial LiDAR. Rem. Sens. 11, 1915. https://doi.org/10.3390/rs11161915.
Schutz, B.E., Zwally, H.J., Shuman, C.A., Hancock, D., DiMarzio, J.P., 2005. Overview of the ICESat mission. Geophys. Res. Lett. 32 https://doi.org/10.1029/2005gl024009.
Silvestri, S., Knight, R., Viezzoli, A., Richardson, C.J., Anshari, G.Z., Dewar, N., Flanagan, N., Comas, X., 2019. Quantification of peat thickness and stored carbon at the landscape scale in tropical peatlands: a comparison of airborne geophysics and an empirical topographic method. J. Geophys. Res.-Earth 124, 3107–3123. https://doi.org/10.1029/2019jf005273.
Simpson, J., Wooster, M., Smith, T., Trivedi, M., Vernimmen, R., Dedi, R., Shakti, M., Dinata, Y., 2016. Tropical peatland burn depth and combustion heterogeneity assessed using UAV photogrammetry and airborne LiDAR. Rem. Sens. 8, 1000. https://doi.org/10.3390/rs8121000.
Sithole, G., Vosselman, G., 2004. Experimental comparison of filter algorithms for bare-Earth extraction from airborne laser scanning point clouds. ISPRS J. Photogrammetry Remote Sens. 59, 85–101. https://doi.org/10.1016/j.isprsjprs.2004.05.004.
Spracklen, B., Spracklen, D.V., 2021. Determination of structural characteristics of old-growth forest in Ukraine using spaceborne LiDAR. Rem. Sens. 13, 1233. https://doi.org/10.3390/rs13071233.
Tang, H., Armston, J., 2019. Algorithm Theoretical Basis Document (ATBD) for GEDI L2B Footprint Canopy Cover and Vertical Profile Metrics. Technical Report. National Aeronautics and Space Administration. Goddard Space Flight Center, Greenbelt, Maryland, USA. Version 1.0.
Tang, H., Brolly, M., Zhao, F., Strahler, A.H., Schaaf, C.L., Ganguly, S., Zhang, G., Dubayah, R., 2014. Deriving and validating leaf area index (LAI) at multiple spatial scales through lidar remote sensing: a case study in Sierra National Forest, CA. Remote Sens. Environ. 143, 131–141. https://doi.org/10.1016/j.rse.2013.12.007.
Vernimmen, R., Hooijer, A., Akmalia, R., Fitranatanegara, N., Mulyadi, D., Yuherdha, A., Andreas, H., Page, S., 2020. Mapping deep peat carbon stock from a LiDAR based DTM and field measurements, with application to eastern Sumatra. Carbon Bal. Manag. 15 https://doi.org/10.1186/s13021-020-00139-2.
Vernimmen, R., Hooijer, A., Yuherdha, A.T., Visser, M., Pronk, M., Eilander, D., Akmalia, R., Fitranatanegara, N., Mulyadi, D., Andreas, H., Ouellette, J., Hadley, W., 2019. Creating a lowland and peatland landscape digital terrain model (DTM) from interpolated partial coverage LiDAR data for Central Kalimantan and East Sumatra, Indonesia. Rem. Sens. 11, 1152. https://doi.org/10.3390/rs11101152.
Vosselman, G., 2000. Slope based filtering of laser altimetry data. Int. J. Appl. Earth Obs. Geoinf. 33, 935–942.
Wake, S., Ramos-Izquierdo, L.A., Eegholm, B.H., Dogoda, P.J., Denny, Z.H., Hersh, M., Mulloney, M.M., Thomes, W.J., Ott, M.N., Jakeman, H., Poulios, D., Mule, P., de Leon, E., Blair, J.B., 2019. Optical system design and integration of the global ecosystem dynamics investigation lidar. In: Strojnik, M., Arnold, G.E. (Eds.), Infrared Remote Sensing and Instrumentation XXVII. https://doi.org/10.1117/12.2530653.
Warren, M., Hergoualc'h, K., Kauffman, J.B., Murdiyarso, D., Kolka, R., 2017. An appraisal of Indonesia's immense peat carbon stock using national peatland maps: uncertainties and potential losses from conversion. Carbon Bal. Manag. 12 https://doi.org/10.1186/s13021-017-0080-2.
Warren, M.W., Kauffman, J.B., Murdiyarso, D., Anshari, G., Hergoualc'h, K., Kurnianto, S., Purbopuspito, J., Gusmayanti, E., Afifudin, M., Rahajoe, J., Alhamd, L., Limin, S., Iswandi, A., 2012. A cost-efficient method to assess carbon stocks in tropical peat soil. Biogeosciences 9, 4477–4485. https://doi.org/10.5194/bg-9-4477-2012.
Xiang, J., Li, H., Zhao, J., Cai, X., Li, P., 2021. Inland water level measurement from spaceborne laser altimetry: validation and comparison of three missions over the Great Lakes and lower Mississippi River. J. Hydrol. 597, 126312 https://doi.org/10.1016/j.jhydrol.2021.126312.
Xing, Y., Huang, J., Gruen, A., Qin, L., 2020. Assessing the performance of ICESat-2/ATLAS multi-channel photon data for estimating ground topography in forested terrain. Rem. Sens. 12, 2084. https://doi.org/10.3390/rs12132084.
Zhang, K., Chen, S.C., Whitman, D., Shyu, M.L., Yan, J., Zhang, C., 2003. A progressive morphological filter for removing nonground measurements from airborne LIDAR data. IEEE Trans. Geosci. Rem. Sens. 41, 872–882. https://doi.org/10.1109/tgrs.2003.810682.
Zhang, W., Qi, J., Wan, P., Wang, H., Xie, D., Wang, X., Yan, G., 2016. An easy-to-use airborne LiDAR data filtering method based on cloth simulation. Rem. Sens. 8, 501. https://doi.org/10.3390/rs8060501.
Zhao, X., Guo, Q., Su, Y., Xue, B., 2016. Improved progressive TIN densification filtering algorithm for airborne LiDAR data in forested areas. ISPRS J. Photogrammetry Remote Sens. 117, 79–91. https://doi.org/10.1016/j.isprsjprs.2016.03.016.